Physics of Fluids

Three-dimensional high-order least square-based finite difference-finite volume method on unstructured grids

Cite as: Phys. Fluids **32**, 123604 (2020); https://doi.org/10.1063/5.0032089
Submitted: 06 October 2020 . Accepted: 17 November 2020 . Published Online: 07 December 2020

Y. Y. Liu (刘阳阳), L. M. Yang (杨锂铭), C. Shu (舒昌), and H. W. Zhang (张黄伟)

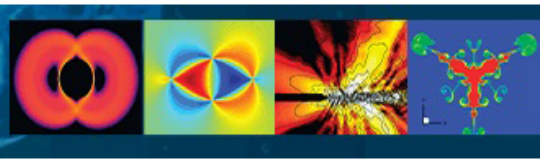

Physics of Fluids ARTICLE scitation.org/journal/phf

Three-dimensional high-order least square-based finite difference-finite volume method on unstructured grids

Cite as: Phys. Fluids 32, 123604 (2020); doi: 10.1063/5.0032089
Submitted: 6 October 2020 • Accepted: 17 November 2020 •
Published Online: 7 December 2020

Y. Y. Liu (刘阳阳), L. M. Yang (杨锂铭), C. Shu (舒昌),[a] and H. W. Zhang (张黄伟)

AFFILIATIONS

Department of Mechanical Engineering, National University of Singapore, 10 Kent Ridge Crescent, Singapore, 119260

Note: This paper is part of the Special Issue on the Lattice Boltzmann Method.
[a]**Author to whom correspondence should be addressed:** mpeshuc@nus.edu.sg

ABSTRACT

The least square-based finite difference-finite volume (LSFD-FV) method has been developed and successfully applied to solve various two-dimensional flow problems with a high-order of accuracy. In this paper, the extension of the LSFD-FV method to the three-dimensional (3D) case on unstructured grids is presented. Different from other existing high-order methods, the LSFD-FV method combines the good features of the least square-based finite difference (LSFD) scheme for derivative approximation and the finite volume (FV) discretization for conservation of physical laws. Within each control cell, a high-order polynomial resultant from a Taylor series expansion is used to approximate the solution in the FV discretization of governing equations, where the derivatives are approximated by the LSFD scheme. As a result, the mesh-free nature of the LSFD scheme endows the LSFD-FV method with the flexibility on unstructured grids. Additionally, the straightforward algorithm of the LSFD scheme and the direct utilization of the Taylor series polynomial make the LSFD-FV method user-friendly and easy to implement. Furthermore, the inviscid and viscous fluxes are simultaneously evaluated by lattice Boltzmann and gas kinetic flux solvers in this work, which avoids additional and complicated treatment for the viscous discretization. Accuracy studies on unstructured hexahedral and tetrahedral grids validate the third-order of accuracy of the 3D LSFD-FV method. Various 3D incompressible and compressible numerical experiments are also presented. The results show that the proposed method enjoys the higher accuracy than the conventional second-order method on the same mesh. When the same accuracy is achieved, the present high-order method has superior computational efficiency to the second-order counterpart.

I. INTRODUCTION

The past decades have witnessed the tremendous advances of computational fluid dynamics (CFD). Plenteous numerical methods have been developed for solving various flow problems in industrial applications. Among them, the high-order methods enjoy increasing popularity due to their higher accuracy and lower dissipation than the conventional second-order methods. Their superior performance is especially demonstrated in studying aeroacoustics, vortex-dominant flows, and turbulent flows. Generally, it is easier to develop a high-order numerical method on structured grids than on unstructured grids. The high-order finite difference (FD),[1–4] essentially non-oscillatory (ENO),[5] and weighted essentially non-oscillatory (WENO)[6] methods are good examples developed on structured grids. However, the structured grid-based methods alone are not easy for engineering applications and some techniques would be required for complex geometry problems. For example, Ref. 7 applied the immersed boundary method with the Runge–Kutta discontinuous Galerkin method to solve two-dimensional flows with complex geometry on structured grids. For complex configurations in the three-dimensional (3D) case, it is usually difficult and time-consuming to generate structured grids, whereas unstructured grids can be generated with ease. As a result, great flexibility of the unstructured grids in handling complex geometries stimulates the

development of unstructured high-order methods. In this work, we also focus on developing a 3D high-order method on unstructured grids.

Over the last two decades, intensive efforts have been made to develop unstructured high-order methods. Typical examples in the literature include finite volume (FV) methods,[8–17] discontinuous Galerkin (DG) methods,[18–22] spectral volume (SV)[23–25] methods, spectral difference (SD)[26,27] methods, etc. These methods differ in terms of the high-order spatial discretization and thus possess distinct characteristics. A detailed review of them can be found in Ref. 28. Among the high-order methods mentioned above, the high-order FV methods draw much attention. Due to the popularization of the FV discretization and the well-developed numerical techniques (e.g., shock capturing technique and time marching strategy) on unstructured grids, the present high-order method is developed in the FV framework.

When considering a numerical method for the practical 3D engineering problems, the complexity of the high-order spatial discretization is significantly important. It determines whether the newly developed high-order method would be widely used or not. Recently, Liu and his co-workers proposed a straightforward and user-friendly high-order FV method on unstructured grids in two dimensions, called least square-based finite difference-finite volume (LSFD-FV) method.[29] The LSFD-FV method directly applies a Taylor series expansion within each control cell to approximate the solution with the high-order accuracy. The unknown coefficients in the approximation polynomial, i.e., the spatial derivatives, are determined by the mesh-free least square-based finite difference (LSFD) scheme using the solutions at centers of the current cell and its neighboring cells. The LSFD method[31,32] is a simple and mesh-free method for derivative approximation at randomly distributed points. Thus, it is an ideal approach to approximate derivatives on unstructured grids. However, due to the nature of the FD discretization, its numerical discretization cannot be guaranteed to be conservative. The FV discretization, unlike the FD method, can remain conservative at the cell and the global level. The LSFD-FV method embeds the LSFD scheme into the framework of the FV method, which provides a simple and effective high-order solver on unstructured mesh. Various two-dimensional applications[29,30] of the LSFD-FV method, such as the incompressible isothermal and thermal flows, and the compressible inviscid and viscous flows, have been made. It is shown that the high-order LSFD-FV method achieves superior accuracy and computational efficiency compared with the k-exact method of the same accuracy order and the second-order method. Therefore, in the present study, the LSFD-FV method is further extended to solve the 3D incompressible and compressible flow problems on unstructured grids.

Apart from the spatial discretization, the flux evaluation also plays a vital role in the high-order solver. In the literature, many high-order methods use the Riemann solver and average approach to evaluate the inviscid and viscous fluxes, respectively. However, for viscous fluxes, the average approach, which takes a simple arithmetic mean of the gradients from the left and right cells of the interface, is inconsistent. It does not consider a possible jump of solutions and may result in a wrong solution.[33] Numerous studies have been conducted for the proper treatment of viscous fluxes, such as the interior penalty approach,[34] the local DG approach,[35] and the second Bassi–Rebay scheme.[36,37] Nevertheless, how to reduce the computational cost or achieve the good convergence is still an open problem. In this work, for viscous flow problems, the viscous and inviscid fluxes are evaluated simultaneously, and different flux solvers are used for the incompressible flow and compressible flow to achieve better efficiency. Particularly, the lattice Boltzmann flux solver (LBFS)[38] is adopted for incompressible isothermal and thermal flows, and the discrete gas-kinetic flux solver (DGKFS)[41] is applied for simulation of compressible viscous flows. These two flux solvers, respectively, use the local solution of the lattice Boltzmann equation and continuous Boltzmann equation to construct the numerical flux at the cell interface. By using such a physical treatment for the evaluation of the numerical flux, the present 3D LSFD-FV method seems to be competitive for simulating viscous flow problems.

A series of incompressible and compressible numerical tests are conducted on unstructured grids to assess the accuracy, efficiency, and robustness of the present 3D high-order LSFD-FV method. Numerical results demonstrate that this high-order method has the third-order of accuracy and it outperforms the conventional low-order methods in terms of the accuracy and computational efficiency.

II. THREE-DIMENSIONAL HIGH-ORDER LEAST SQUARE-BASED FINITE DIFFERENCE-FINITE VOLUME (LSFD-FV) METHOD

A. Governing equations and high-order finite volume discretization

N–S equations are considered for a general case and discretized by the FV method, where the conservative variables are defined at cell centers. In the 3D case, the semi-discrete form of the N–S equations discretized by the cell-centered FV method can be cast as

$$\frac{d}{dt}\left(\int_{\Omega_i} \boldsymbol{U} d\Omega\right) = -\sum_{j=1}^{Nf}\sum_{GQp=1}^{nGQp} \left(\boldsymbol{F}_{n,GQp} A\right)_j w_{GQp} + \int_{\Omega_i} \boldsymbol{Q} d\Omega, \quad (1)$$

with

$$\boldsymbol{U} = \left[\rho, \rho u_x, \rho u_y, \rho u_z, \rho E\right]^T, \quad (2)$$

where $\boldsymbol{U}$ is the vector of conservative variables and $\boldsymbol{F}_n$ represents the flux vector in the Cartesian coordinate system. Note that the Gaussian quadrature has been applied for the high-order accurate computation of the integral of fluxes at the cell interface. Nf is the number of cell faces of the control volume Ω_i. $nGQp$, A, and w_{GQP} are the same as those in Ref. 29. ρ, $\boldsymbol{u} = (u_x, u_y, u_z)$, and E are, respectively, the density, velocity, and total energy of the fluid flow. $E = e + (u_x^2 + u_y^2 + u_z^2)/2$, where $e = p/[(\gamma - 1)\rho]$ is the internal energy of the mean flow. p is the pressure, and γ is the specific heat ratio. The source term $\boldsymbol{Q}$, which comprises all volume sources due to body sources and volumetric heating, can be calculated directly from the conservative variables at cell centers.

In order to obtain higher-order numerical solutions of flow variables, the present high-order LSFD-FV method applies a Taylor series expansion at the cell center with the designed order of accuracy. For instance, the following polynomial approximates the solution variable at the location (x, y, z) with the third-order of accuracy,

$$\begin{aligned}\boldsymbol{U}(x,y,z) = \boldsymbol{U}_i &+ \frac{\partial \boldsymbol{U}}{\partial x}|_i (x-x_i) + \frac{\partial \boldsymbol{U}}{\partial y}|_i (y-y_i) + \frac{\partial \boldsymbol{U}}{\partial z}|_i (z-z_i) \\ &+ \frac{\partial^2 \boldsymbol{U}}{\partial x^2}|_i \frac{(x-x_i)^2}{2} + \frac{\partial^2 \boldsymbol{U}}{\partial y^2}|_i \frac{(y-y_i)^2}{2} + \frac{\partial^2 \boldsymbol{U}}{\partial z^2}|_i \frac{(z-z_i)^2}{2} \\ &+ \frac{\partial^2 \boldsymbol{U}}{\partial x \partial y}|_i (x-x_i)(y-y_i) + \frac{\partial^2 \boldsymbol{U}}{\partial x \partial z}|_i (x-x_i)(z-z_i) \\ &+ \frac{\partial^2 \boldsymbol{U}}{\partial y \partial z}|_i (y-y_i)(z-z_i), \end{aligned} \tag{3}$$

where the reference point (x_i, y_i, z_i) is the cell centroid of Ω_i. Based on this high-order Taylor polynomial, the solution at the quadrature points along the cell interface is interpolated with the third-order of accuracy. This provides the basis for high-order accurate evaluation of numerical fluxes. When Eq. (3) is substituted into the volume integral in Eq. (1), the following equation can be obtained,

$$\int_{\Omega_i} \boldsymbol{U}(x,y) d\Omega = \Omega_i \boldsymbol{U}_i + d\boldsymbol{U}_i^T C_i = \Omega_i \boldsymbol{U}_i + \sum_{k=1}^{N_i} C_i^k d\boldsymbol{U}_i^k, \tag{4}$$

with

$$\begin{aligned} d\boldsymbol{U}_i^T &= \left[\frac{\partial \boldsymbol{U}}{\partial x}|_i, \frac{\partial \boldsymbol{U}}{\partial y}|_i, \frac{\partial \boldsymbol{U}}{\partial z}|_i, \frac{\partial^2 \boldsymbol{U}}{\partial x^2}|_i, \frac{\partial^2 \boldsymbol{U}}{\partial y^2}|_i, \frac{\partial^2 \boldsymbol{U}}{\partial z^2}|_i, \frac{\partial^2 \boldsymbol{U}}{\partial x \partial y}|_i, \frac{\partial^2 \boldsymbol{U}}{\partial x \partial z}|_i, \frac{\partial^2 \boldsymbol{U}}{\partial y \partial z}|_i \right], \\ C_i^T &= \left[\overline{\overline{x^1 y^0 z^0}}_i, \overline{\overline{x^0 y^1 z^0}}_i, \overline{\overline{x^0 y^0 z^1}}_i, \frac{\overline{\overline{x^2 y^0 z^0}}_i}{2}, \frac{\overline{\overline{x^0 y^2 z^0}}_i}{2}, \frac{\overline{\overline{x^0 y^0 z^2}}_i}{2}, \overline{\overline{x^1 y^1 z^0}}_i, \overline{\overline{x^1 y^0 z^1}}_i, \overline{\overline{x^0 y^1 z^1}}_i \right]. \end{aligned} \tag{5}$$

where $\overline{\overline{x^n y^m z^l}}_i = \int_{\Omega_i} (x-x_i)^n (y-y_i)^m (z-z_i)^l d\Omega$. The coefficients C_i represent the volume integral of the distance relations with respect to the cell center and they could be diverse for different cells in the whole flow domain. Note that Eq. (4) involves the solution $\boldsymbol{U}_i$ at the cell center and its N_i unknown spatial derivatives $d\boldsymbol{U}_i$. As shown in Eq. (5), N_i is 9 when the third-order of accuracy is expected. In this work, $d\boldsymbol{U}_i$ are approximated by the mesh-free LSFD method[31,32] by using the solutions at the centers of current cell i and its N neighboring cells, i.e.,

$$d\boldsymbol{U}_i^k = \sum_{j=1}^{N} W_{k,j}^i (\boldsymbol{U}_{ij} - \boldsymbol{U}_i), k = 1, \ldots, 9, \tag{6}$$

where $\boldsymbol{U}_{ij}$ denotes the solution value at the center of the jth neighboring cell to the current cell i. The details of how to determine the coefficients $W_{k,j}^i$ will be presented in Sec. II B. With Eqs. (4) and (6), Eq. (1) is rewritten as

$$\left(\Omega_i - \sum_{k=1}^{9} C_i^k \sum_{j=1}^{N} W_{k,j}^i \right) \frac{\partial \boldsymbol{U}_i}{\partial t} + \left(\sum_{k=1}^{9} C_i^k \sum_{j=1}^{N} W_{k,j}^i \right) \frac{\partial \boldsymbol{U}_{ij}}{\partial t} = -\boldsymbol{R}_i, \tag{7}$$

where $\boldsymbol{R}_i$ denotes the discrete form of the right-hand side of Eq. (1). In this work, the numerical fluxes in $\boldsymbol{R}_i$ are evaluated by the specific flux solver for different flow problems, which will be described in Sec. II C. After applying Eq. (7) to all control cells in the flow domain, the following matrix form can be obtained,

$$\mathbf{M} \frac{d\mathbf{U}}{dt} = -\mathbf{R}, \tag{8}$$

where $\mathbf{U}$ represents the solution vector composed by all control cells and $\mathbf{M}$ is a sparse coefficient matrix formed by coefficients on the left-hand side of Eq. (7). To solve the resultant ordinary differential equations efficiently, the implicit time marching techniques are adopted.

B. Derivative approximation by least square-based finite difference (LSFD) scheme

In this work, we apply the LSFD method[31,32] to approximate the spatial derivatives in Eq. (3). Since the number of unknowns is 9, the same number of equations is required to construct a well-posed system. Therefore, Eq. (3) is applied to 9 neighboring cells and a linear system can be obtained as follows:

$$\hat{\boldsymbol{S}} d\boldsymbol{U} = \Delta \hat{\boldsymbol{U}}, \tag{9}$$

with $\hat{\boldsymbol{S}}$ and $\Delta \hat{\boldsymbol{U}}$ given by

$$\hat{\boldsymbol{S}} = \begin{pmatrix} \Delta x_1 & \Delta y_1 & \Delta z_1 & \frac{\Delta x_1^2}{2} & \frac{\Delta y_1^2}{2} & \frac{\Delta z_1^2}{2} & \Delta x_1 \Delta y_1 & \Delta x_1 \Delta z_1 & \Delta y_1 \Delta z_1 \\ \Delta x_2 & \Delta y_2 & \Delta z_2 & \frac{\Delta x_2^2}{2} & \frac{\Delta y_2^2}{2} & \frac{\Delta z_2^2}{2} & \Delta x_2 \Delta y_2 & \Delta x_2 \Delta z_2 & \Delta y_2 \Delta z_2 \\ \vdots & \vdots & \vdots & \vdots & \vdots & \vdots & \vdots & \vdots & \vdots \\ \Delta x_9 & \Delta y_9 & \Delta z_9 & \frac{\Delta x_9^2}{2} & \frac{\Delta y_9^2}{2} & \frac{\Delta z_9^2}{2} & \Delta x_9 \Delta y_9 & \Delta x_9 \Delta z_9 & \Delta y_9 \Delta z_9 \end{pmatrix}, \tag{10}$$

$$\Delta \hat{\boldsymbol{U}}^T = [\boldsymbol{U}_{i1} - \boldsymbol{U}_i, \boldsymbol{U}_{i2} - \boldsymbol{U}_i, \ldots, \boldsymbol{U}_{i9} - \boldsymbol{U}_i],$$

where $(\Delta x_j, \Delta y_j, \Delta z_j) = (x_j - x_i, y_j - y_i, z_j - z_i)$. Through the equation system (9), the derivative vector $d\boldsymbol{U}$ can be solved in terms of $\Delta \hat{\boldsymbol{U}}$. In practice, the equation system may be ill-conditioned or even singular due to unstructured cell distribution for a general case. To overcome this difficulty, the least square optimization and local scaling technique are used. In addition, the distance-related weighting function

is also introduced to reduce the influence of data farther from the reference point. Since the basic idea and procedures of such techniques have been given in Refs. 29 and 30, the details are omitted here. Finally, the derivative vector $d\boldsymbol{U}$ can be calculated by

$$d\boldsymbol{U} = \boldsymbol{W}\Delta\boldsymbol{U}, \tag{11}$$

where $\boldsymbol{W}$ is a $9 \times N$ dimensional weighting coefficient matrix and it is uniquely determined by the coordinates of mesh points (centers of the current cell and its neighboring cells). In practical implementation, $\boldsymbol{W}$ is calculated once and stored for problems with the fixed computational mesh. This saves computational effort.

C. Evaluation of numerical flux

Subsection II B addresses the derivative approximation in the high-order LSFD-FV method. After obtaining the various derivatives in Eq. (3), the flow variables at the cell interface can be interpolated with the third-order of accuracy. Based on this, accurate evaluation of the numerical flux at the cell interface is discussed in this subsection. In this work, three kinds of flux solvers are applied to compute the flux physically. For incompressible isothermal and thermal flows, the LBFS[38] is adopted and it can evaluate the inviscid and viscous fluxes simultaneously by local reconstruction of lattice Boltzmann solution. For compressible inviscid flows, the compressible LBFS[39,40] based on the non-free parameter D1Q4 model is used to compute the inviscid flux at the cell interface. In the simulation of compressible viscous flows, the DGKFS[41] is applied for simultaneous evaluation of the inviscid and viscous fluxes by the local solution of the continuous Boltzmann equation. These flux solvers have been applied in many problems[42–44] and have shown good features, such as excellent computational efficiency and easy implementation. Therefore, with applying them for specific flow problems, the present high-order solver would present a competitive performance in simulating various incompressible and compressible flows.

For simplicity, the development and derivation of the above flux solvers are briefly reviewed. Special attention is paid to their implementation in the present solver and effect on the overall accuracy. To apply these flux solvers in the present 3D unstructured LSFD-FV method with ease, a local coordinate system is introduced at the cell interface. In such a local coordinate system, the directions are the outward normal direction and two tangential directions of the cell interface, which are, respectively, denoted by the subscripts "1," "2," and "3." Details of these three flux solvers in the local coordinate system are shown below.

First, the LBFS for both isothermal and thermal incompressible flows is introduced. Following the work of Wang *et al.*,[38] the N–S equations can be recovered through multiscale Chapman–Enskog expansion analysis to the thermal lattice Boltzmann equation in the low Mach number limit, which gives the interface flux $\boldsymbol{F} = (F_1, F_2, F_3, F_4, F_5)^T$ in the local coordinate system as follows:

$$\begin{aligned}
F_1 &= \sum_{\alpha=0}^{Nd} (\boldsymbol{e}_\alpha)_1 f_\alpha^{eq},\\
F_2 &= \sum_{\alpha=0}^{Nd} (\boldsymbol{e}_\alpha)_1 (\boldsymbol{e}_\alpha)_1 \left[f_\alpha^{eq} + (1 - 1/2\tau_v) f_\alpha^{neq}\right],\\
F_3 &= \sum_{\alpha=0}^{Nd} (\boldsymbol{e}_\alpha)_1 (\boldsymbol{e}_\alpha)_2 \left[f_\alpha^{eq} + (1 - 1/2\tau_v) f_\alpha^{neq}\right],\\
F_4 &= \sum_{\alpha=0}^{Nd} (\boldsymbol{e}_\alpha)_1 (\boldsymbol{e}_\alpha)_3 \left[f_\alpha^{eq} + (1 - 1/2\tau_v) f_\alpha^{neq}\right],\\
F_5 &= \sum_{\alpha=0}^{Nd} (\boldsymbol{e}_\alpha)_1 \left[g_\alpha^{eq} + (1 - 1/2\tau_\kappa) g_\alpha^{neq}\right],
\end{aligned} \tag{12}$$

where $\boldsymbol{e}_\alpha$ is the lattice velocity vector, and the single relaxation parameters τ_v and τ_κ are, respectively, related to the dynamic viscosity and thermal diffusivity. f_α^{eq} denotes the equilibrium density distribution function along the α direction, and f_α^{neq} is the corresponding non-equilibrium distribution function. g_α^{eq} denotes the equilibrium internal energy distribution function along the α direction, and g_α^{neq} is the corresponding non-equilibrium distribution function. $Nd + 1$ is the number of discrete particle velocities in the lattice Boltzmann model. In the present study, the commonly used D3Q15 lattice model ($Nd + 1 = 15$) is applied and the corresponding f_α^{eq} and g_α^{eq} are referred to Ref. 38. τ_v and τ_κ in Eq. (12) are determined from the kinematic viscosity v and thermal diffusivity κ by

$$v = (\tau_v - 1/2) c_s^2 \delta_t, \tag{13}$$

$$\kappa = \left[5(\tau_\kappa - 1/2) {c_s}^2 \delta_t\right]/3, \tag{14}$$

where δ_t denotes the streaming time step, which equals the lattice spacing, and c_s is the sound speed. The non-equilibrium distribution functions f_α^{neq} and g_α^{neq} are approximated by

$$f_\alpha^{neq}(\boldsymbol{r}, t) = -\tau_v \left[f_\alpha^{eq}(\boldsymbol{r}, t) - f_\alpha^{eq}(\boldsymbol{r} - \boldsymbol{e}_\alpha\delta_t, t - \delta_t)\right] + O\left(\delta_t^2\right), \tag{15}$$

$$g_\alpha^{neq}(\boldsymbol{r}, t) = -\tau_\kappa \left[g_\alpha^{eq}(\boldsymbol{r}, t) - g_\alpha^{eq}(\boldsymbol{r} - \boldsymbol{e}_\alpha\delta_t, t - \delta_t)\right] + O\left(\delta_t^2\right), \tag{16}$$

where $\boldsymbol{r}$ is the physical location of the Gaussian quadrature point along the cell interface and t is the time. $f_\alpha^{eq}(\boldsymbol{r}, t)$ and $f_\alpha^{eq}(\boldsymbol{r} - \boldsymbol{e}_\alpha\delta_t, t - \delta_t)$ are the equilibrium density distribution functions at $\boldsymbol{r}$ and its surrounding nodes $\boldsymbol{r} - \boldsymbol{e}_\alpha\delta_t$, respectively. $g_\alpha^{eq}(\boldsymbol{r}, t)$ and $g_\alpha^{eq}(\boldsymbol{r} - \boldsymbol{e}_\alpha\delta_t, t - \delta_t)$ are the equilibrium internal energy distribution functions at the corresponding locations.

To calculate $f_\alpha^{neq}(\boldsymbol{r}, t)$ and $g_\alpha^{neq}(\boldsymbol{r}, t)$, the flow variables at the location $\boldsymbol{r} - \boldsymbol{e}_\alpha\delta_t$ are interpolated first by using Eq. (3) with the third-order of accuracy based on the information at cell centroids $\boldsymbol{r}_i$ and $\boldsymbol{r}_j$, i.e.,

$$\boldsymbol{U}(\boldsymbol{r} - \boldsymbol{e}_\alpha\delta_t) = \begin{cases} \boldsymbol{U}(\boldsymbol{r}_i) + \nabla\boldsymbol{U}(\boldsymbol{r}_i)\Delta\boldsymbol{X}_i + \dfrac{1}{2}\Delta\boldsymbol{X}_i^T\boldsymbol{H}(\boldsymbol{X}_i)\Delta\boldsymbol{X}_i + O\left(\Delta X^3\right), & (\boldsymbol{r} - \boldsymbol{e}_\alpha\delta_t) \in \Omega_i, \\ \boldsymbol{U}(\boldsymbol{r}_j) + \nabla\boldsymbol{U}(\boldsymbol{r}_j)\Delta\boldsymbol{X}_j + \dfrac{1}{2}\Delta\boldsymbol{X}_j^T\boldsymbol{H}(\boldsymbol{X}_j)\Delta\boldsymbol{X}_j + O\left(\Delta X^3\right), & (\boldsymbol{r} - \boldsymbol{e}_\alpha\delta_t) \in \Omega_j, \end{cases} \tag{17}$$

with

$$\Delta \boldsymbol{X}_k = \left[\left(\boldsymbol{r} - \boldsymbol{e}_\alpha \delta_t - \boldsymbol{r}_k \right)_x, \left(\boldsymbol{r} - \boldsymbol{e}_\alpha \delta_t - \boldsymbol{r}_k \right)_y, \left(\boldsymbol{r} - \boldsymbol{e}_\alpha \delta_t - \boldsymbol{r}_k \right)_z \right]^T, \quad k = i \text{ or } j. \tag{18}$$

$\nabla \boldsymbol{U}$ and $\boldsymbol{H}$ are given by

$$\nabla \boldsymbol{U} = \left(\frac{\partial \boldsymbol{U}}{\partial x}, \frac{\partial \boldsymbol{U}}{\partial y}, \frac{\partial \boldsymbol{U}}{\partial z} \right), \boldsymbol{H} = \begin{bmatrix} \frac{\partial^2 \boldsymbol{U}}{\partial x^2} & \frac{\partial^2 \boldsymbol{U}}{\partial x \partial y} & \frac{\partial^2 \boldsymbol{U}}{\partial x \partial z} \\ \frac{\partial^2 \boldsymbol{U}}{\partial y \partial x} & \frac{\partial^2 \boldsymbol{U}}{\partial y^2} & \frac{\partial^2 \boldsymbol{U}}{\partial y \partial z} \\ \frac{\partial^2 \boldsymbol{U}}{\partial z \partial x} & \frac{\partial^2 \boldsymbol{U}}{\partial z \partial y} & \frac{\partial^2 \boldsymbol{U}}{\partial z^2} \end{bmatrix}, \tag{19}$$

where the derivatives are approximated by the LSFD method as introduced in Subsection II B. Once the required flow variables are available, all the equilibrium density and internal energy distribution functions in Eqs. (15) and (16) can be computed following the derivations in Ref. 38. In this way, $f_\alpha^{neq}(\boldsymbol{r}, t)$ and $g_\alpha^{neq}(\boldsymbol{r}, t)$ can be, respectively, calculated, and then, the flux vector $\boldsymbol{F} = (F_1, F_2, F_3, F_4, F_5)^T$ in Eq. (12) can be obtained.

As stated previously, the whole flux $\boldsymbol{F}$ is computed in the local coordinate system by the LBFS. However, in the practical calculation, the flux $\boldsymbol{F}_n$ in Eq. (1) is defined in the global coordinate system. Thus, the transformation as the following form should be adopted,

$$\begin{aligned} \boldsymbol{F}_n = (&F_1, F_2 n_{1x} + F_3 n_{2x} + F_4 n_{3x}, F_2 n_{1y} + F_3 n_{2y} + F_4 n_{3y}, \\ &F_2 n_{1z} + F_3 n_{2z} + F_4 n_{3z}, F_5)^T, \end{aligned} \tag{20}$$

where $\boldsymbol{n}_1 = (n_{1x}, n_{1y}, n_{1z})$ is the unit vector in direction "1" of the local coordinate system. $\boldsymbol{n}_2 = (n_{2x}, n_{2y}, n_{2z})$ and $\boldsymbol{n}_3 = (n_{3x}, n_{3y}, n_{3z})$ are, respectively, the unit vectors in directions "2" and "3."

Second, the non-free parameter D1Q4 compressible LBFS[39,40] is introduced to simulate inviscid compressible flows in the present high-order method. For simplicity, it is hereinafter referred to as the D1Q4 model. In this model, the discrete lattice velocities contain 4 equilibrium distribution functions g_i, $i = 1$–4, and 2 lattice velocities d_1 and d_2. g_i are determined from the moment relationships corresponding to Euler equations, and the lattice velocities are computed from two appended high-order moment relationships. The expressions of g_i, d_1, and d_2 can refer to Refs. 39 and 40. Following the work of Yang *et al.*,[40] the inviscid flux at the cell interface can be expressed as

$$\begin{aligned} \boldsymbol{F} &= \sum_{i=1}^{4} \xi_i \boldsymbol{\phi}_a g_i(\boldsymbol{r}, t) + \tau_0 \left[\sum_{i=1}^{4} \xi_i \boldsymbol{\phi}_a g_i(\boldsymbol{r} - \xi_i \delta_t, t - \delta_t) - \sum_{i=1}^{4} \xi_i \boldsymbol{\phi}_a g_i(\boldsymbol{r}, t) \right] \\ &= \boldsymbol{F}_c^I + \tau_0 \left[\boldsymbol{F}_c^{II} - \boldsymbol{F}_c^I \right], \end{aligned} \tag{21}$$

where τ_0 is the dimensionless relaxation time and ξ_i is the lattice velocity in the i direction. Generally, $\tau_0 = \tanh[10(|p_L - p_R|)/(p_L + p_R)]$, where $\tanh(x)$ is the hyperbolic tangent function, and p_L and p_R are the pressure at the left and right sides of the cell interface. When strong shock waves are considered, a switch function is introduced and the details can be found in Ref. 40. $\boldsymbol{\phi}_a$ represents the moment vector, which can be written as

$$\boldsymbol{\phi}_a = \left(1, \xi_i n_{1x} + u_{\tau x}, \xi_i n_{1y} + u_{\tau y}, \xi_i n_{1z} + u_{\tau z}, \left(\xi_i^2 + |\boldsymbol{u}_\tau|^2 \right)/2 + e_p \right)^T, \tag{22}$$

where $e_p = [1 - (\gamma - 1)/2]e$ refers to the potential energy of particles and the tangential velocity vector is $\boldsymbol{u}_\tau = (u_{\tau x}, u_{\tau y}, u_{\tau z}) = \boldsymbol{u} - u_1 \boldsymbol{n}_1$. It is clear in Eq. (21) that the total inviscid flux consists of the fluxes attributed to the equilibrium distribution functions at the cell interface $g_i(\boldsymbol{r}, t)$ and at the surrounding points of the cell interface $g_i(\boldsymbol{r} - \xi_i \delta_t, t - \delta_t)$. We can calculate $g_i(\boldsymbol{r} - \xi_i \delta_t, t - \delta_t)$ according to the location of $\boldsymbol{r} - \xi_i \delta_t$ as follows:

$$g_i(\boldsymbol{r} - \xi_i \delta_t, t - \delta_t) = \begin{cases} g_i^L, & i = 1, 3, \\ g_i^R, & i = 2, 4, \end{cases} \tag{23}$$

where g_i^L and g_i^R denote the equilibrium distribution functions at the left and right sides of the cell interface, which are calculated from the corresponding conservative variables based on the expressions of g_i. In the present high-order method, these conservative variables are interpolated by the way like Eq. (17) with the third-order of accuracy. If there exists the discontinuity, the shock-capturing technique would be used during the interpolation process. The conservative variables at the cell interface are then computed by

$$\boldsymbol{U}(\boldsymbol{r}, t) = \sum_{i=1,3} \boldsymbol{\phi}_a g_i^L + \sum_{i=2,4} \boldsymbol{\phi}_a g_i^R. \tag{24}$$

With Eq. (24), the primitive variables ρ, u_1, $\boldsymbol{u}_\tau$, p at the cell interface used to compute $g_i(\boldsymbol{r}, t)$ can be obtained. Once $g_i(\boldsymbol{r}, t)$ and $g_i(\boldsymbol{r} - \xi_i \delta_t, t - \delta_t)$ are both available, the flux $\boldsymbol{F}_c^I$ and $\boldsymbol{F}_c^{II}$ can be computed explicitly via the following equations:

$$\boldsymbol{F}_c^I = \begin{bmatrix} \rho u_1 \\ (\rho u_1 u_1 + p) n_{1x} + \rho u_1 u_{\tau x} \\ (\rho u_1 u_1 + p) n_{1y} + \rho u_1 u_{\tau y} \\ (\rho u_1 u_1 + p) n_{1z} + \rho u_1 u_{\tau z} \\ (\rho (u_1 u_1/2 + e) + p) u_1 + \rho u_1 |\boldsymbol{u}_\tau|^2/2 \end{bmatrix}, \tag{25}$$

$$\boldsymbol{F}_c^{II} = \sum_{i=1,3} \xi_i \boldsymbol{\phi}_a g_i^L + \sum_{i=2,4} \xi_i \boldsymbol{\phi}_a g_i^R. \tag{26}$$

The whole flux $\boldsymbol{F}$ in the local coordinate system is finally computed by Eq. (21). As stated previously, the flux $\boldsymbol{F}_n$ in Eq. (1), which is defined in the global coordinate system, can be obtained via Eq. (20).

Finally, the DGKFS[41] adopted in this high-order LSFD-FV method for compressible viscous flows is presented. In the DGKFS, the D3Q8 discrete velocity model is applied. It defines eight discrete points on a spherical surface with the radius c and center $\boldsymbol{u} = (u_1, u_2, u_3)$. Since the moment integrations to recover N–S equations by the continuum Boltzmann equation can be accurately replaced with the integral quadrature, the conservative variables and numerical fluxes can be computed by the weighted summation of distribution functions with the D3Q8 model. The formulations of the equilibrium distribution functions g_q and discrete velocities ξ_q are given in Ref. 41. With the D3Q8 model, the fluxes at the cell interface can be computed by the DGKFS as the following numerical integrations:

$$\boldsymbol{F} = \left(F_1, F_2, F_3, F_4, F_5 \right)^T = \sum_{q=1}^{8} \xi_{q,1} \boldsymbol{\phi}_q f_q \Delta S, \tag{27}$$

where $\Delta S = \pi/2$ and $\boldsymbol{\phi}_q$ stands for the moment vector given by

$$\boldsymbol{\phi}_q = \left(1, \xi_{q,1}, \xi_{q,2}, \xi_{q,3}, \frac{1}{2}\left\|\boldsymbol{\xi}_q\right\|^2 + e_{p,q}\right)^T. \quad (28)$$

The distribution function f_q at the cell interface, i.e., $f_q(\boldsymbol{r}, t)$, can be expressed as

$$f_q(\boldsymbol{r}, t) = g_q(\boldsymbol{r}, t) + \tau_0\left[g_q\left(\boldsymbol{r} - \boldsymbol{\xi}_q\delta_t, t - \delta_t\right) - g_q(\boldsymbol{r}, t)\right] + O\left(\delta_t^2\right), \quad (29)$$

where $g_q(\boldsymbol{r}, t)$ and $g_q(\boldsymbol{r} - \boldsymbol{\xi}_q\delta_t, t - \delta_t)$ are, respectively, the equilibrium distribution functions at the cell interface and at the discrete points on the sphere. For convenience, "$(\boldsymbol{r}, t)$" and "$(\boldsymbol{r} - \boldsymbol{\xi}_q\delta_t, t - \delta_t)$" are, respectively, noted by superscripts "*face*" and "*sph*." Substituting Eq. (29) into Eq. (27), the flux vector $\boldsymbol{F}$ can be obtained by

$$\begin{aligned}\boldsymbol{F} &= \sum_{q=1}^{8} \xi_{q,1}^{face} \boldsymbol{\phi}_q^{face} g_q^{face} \Delta S + \tau_0 \left[\sum_{q=1}^{8} \xi_{q,1}^{sph} \boldsymbol{\phi}_q^{sph} g_q^{sph} \Delta S - \sum_{q=1}^{8} \xi_{q,1}^{face} \boldsymbol{\phi}_q^{face} g_q^{face} \Delta S\right] \\ &= \boldsymbol{F}^I + \tau_0\left[\boldsymbol{F}^{II} - \boldsymbol{F}^I\right]. \end{aligned} \quad (30)$$

Clearly, the flux $\boldsymbol{F}$ contains two parts: one is the flux $\boldsymbol{F}^I$ attributed to the equilibrium distribution functions and moments at the cell interface and the other is the flux $\boldsymbol{F}^{II}$ attributed to the equilibrium distribution functions and moments on the spherical surface. The conservative variables at the discrete points on the spherical surface $\boldsymbol{U}_q^{sph}$ are computed like the way in Eq. (17) with $\Delta \boldsymbol{X}_i = \left(\left(\boldsymbol{r} - \boldsymbol{\xi}_q^+\delta_t - \boldsymbol{r}_i\right)_x, \left(\boldsymbol{r} - \boldsymbol{\xi}_q^+\delta_t - \boldsymbol{r}_i\right)_y, \left(\boldsymbol{r} - \boldsymbol{\xi}_q^+\delta_t - \boldsymbol{r}_i\right)_z\right)^T$. $\boldsymbol{\xi}_q^+$ is the predicted particle velocity at the cell interface, and it can be approximated based on the Roe-average.[41] When the flow field is not smooth, the slope limiter would be applied in the interpolation process to suppress the numerical oscillation in the vicinity of discontinuities. Based on $\boldsymbol{U}_q^{sph}$, the particle velocities ξ_q^{sph}, particle potential energy $e_{p,q}^{sph}$, and equilibrium distribution function g_q^{sph} can be computed. Then, the flux $\boldsymbol{F}^{II}$ is obtained by

$$\boldsymbol{F}^{II} = \sum_{q=1}^{8} \xi_{q,1}^{sph} \boldsymbol{\phi}_q^{sph} g_q^{sph} \Delta S = \begin{bmatrix} \sum_{q=1}^{8} \xi_{q,1}^{sph} g_q^{sph} \Delta S \\ \sum_{q=1}^{8} \xi_{q,1}^{sph} \xi_{q,1}^{sph} g_q^{sph} \Delta S \\ \sum_{q=1}^{8} \xi_{q,1}^{sph} \xi_{q,2}^{sph} g_q^{sph} \Delta S \\ \sum_{q=1}^{8} \xi_{q,1}^{sph} \xi_{q,3}^{sph} g_q^{sph} \Delta S \\ \sum_{q=1}^{8} \xi_{q,1}^{sph} \left[\left\|\boldsymbol{\xi}_{q,1}^{sph}\right\|^2/2 + e_{p,q}^{sph}\right] g_q^{sph} \Delta S \end{bmatrix}. \quad (31)$$

According to the compatibility condition, the conservative variables at the cell interface can be computed by

$$\boldsymbol{U}^{face} = \sum_{q=1}^{8} \boldsymbol{\phi}_q^{sph} g_q^{sph} \Delta S. \quad (32)$$

$\boldsymbol{F}^I$ can then be calculated by substituting the conservative variables $\boldsymbol{U}^{face}$ directly into the expression of inviscid flux, i.e.,

$$\boldsymbol{F}^I = \begin{bmatrix} \rho u_1 \\ \rho u_1 u_1 + p \\ \rho u_1 u_2 \\ \rho u_1 u_3 \\ (\rho E + p) u_1 \end{bmatrix}^{face}. \quad (33)$$

Finally, the whole flux $\boldsymbol{F}$ in the local coordinate system is obtained by Eq. (30), and the flux $\boldsymbol{F}_n$ in the global coordinate system can be computed by Eq. (20).

Up to this point, the three flux solvers and their implementation in the present high-order LSFD-FV method have been introduced. In the flux solvers discussed above, the solution is reconstructed physically and locally at every Gaussian quadrature point along the cell interface. This means that different δ_t could be chosen for different interfaces, which provides great flexibility for application on unstructured grids. Meanwhile, due to the independence between the time marching step Δt and the streaming time step δ_t (δ_t is only used in the solution reconstruction), the choice of small δ_t would not affect the time evolution process in the present method. Basically, in the 3D case, the limitation of δ_t implies that discrete particles/points in the physical space constructed around the Gaussian quadrature point must be within the right and left cells of the interface to avoid extrapolation. In this work, δ_t is determined by

$$\delta_t = \begin{cases} \left(\frac{1}{2} - \frac{1}{2\sqrt{3}}\right) h_{\min}, & LBFS \\ \left[\left(\frac{1}{2} - \frac{1}{2\sqrt{3}}\right) h_{\min}\right] / \left(\max\{u_1^+, u_2^+, u_3^+\} + c^+\right), & DGKFS, \end{cases} \quad (34)$$

where h_{min} is the minimum edge length of the left and right cells of the interface for a hexahedral mesh or the radius of the inscribed sphere in the left and right cells of the interface for a tetrahedral mesh.

III. NUMERICAL RESULTS AND DISCUSSIONS

In this section, the accuracy, computational efficiency, and robustness of the developed high-order LSFD-FV method are assessed by simulating a series of 3D incompressible and compressible benchmark cases. All simulations are done on a PC with 2.30 GHz CPU.

A. Advection of density perturbation problem for accuracy test

First, the advection of density perturbation[45] for the 3D flow is presented to validate the order of accuracy. The initial condition of this problem is set as follows:

$$\begin{aligned} &\rho(x, y, z) = 1 + 0.2\sin(\pi(x + y + z)), \\ &u(x, y, z) = 1, v(x, y, z) = 1, w(x, y, z) = 1, p(x, y, z) = 1. \end{aligned} \quad (35)$$

The exact solution under periodic boundary conditions is

$$\begin{aligned} &\rho(x, y, z, t) = 1 + 0.2\sin(\pi(x + y + z - t)), \\ &u(x, y, z, t) = 1, v(x, y, z, t) = 1, w(x, y, z, t) = 1, p(x, y, z, t) = 1. \end{aligned} \quad (36)$$

Numerical tests are conducted on the computational domain of [0, 2] × [0, 2] × [0, 2]. The uniform hexahedral grids with the

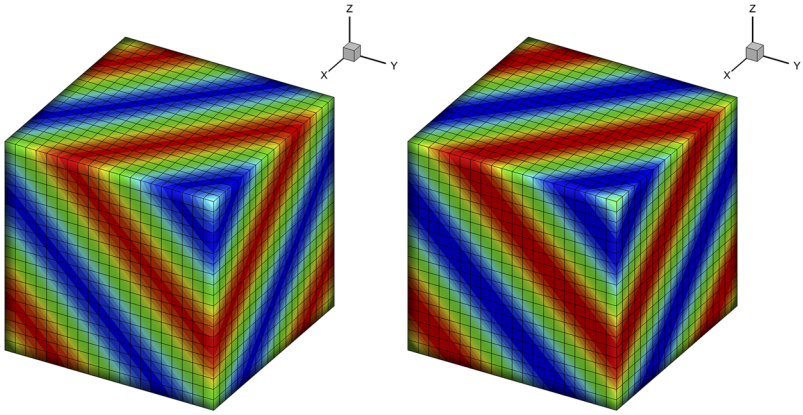

FIG. 1. Density contours obtained by the high-order LSFD-FV method (left) and the exact solutions (right) for the 3D advection of density perturbation on uniform hexahedral meshes with $h = 1/10$.

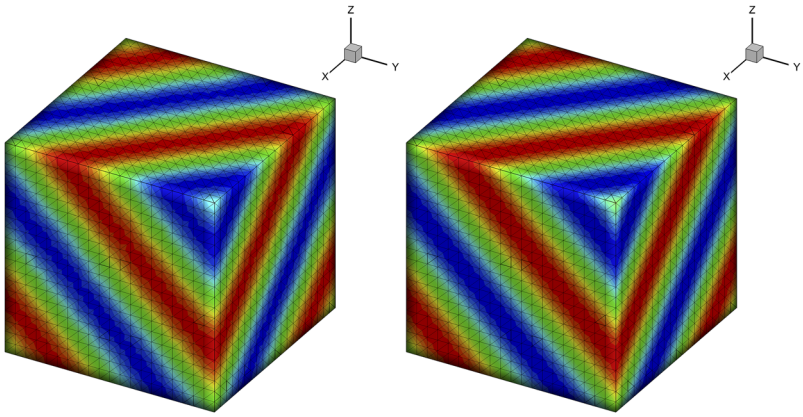

FIG. 2. Density contours obtained by the high-order LSFD-FV method (left) and the exact solutions (right) for the 3D advection of density perturbation on tetrahedral mesh with $h = 1/10$.

mesh size from $h = 1/10$ to $1/30$ and the unstructured tetrahedral grids with almost equivalent mesh size from $h = 1/5$ to $1/15$ are used. Results at $t = 2$ are extracted. The density contours computed by the high-order LSFD-FV method on uniform hexahedral and tetrahedral grids with $h = 1/10$ are, respectively, presented in Figs. 1 and 2, in which good agreements with the analytical solutions are observed. For quantitative comparison, the L_2 errors and convergence orders on the hexahedral and tetrahedral meshes are, respectively, given in Tables I and II. These results show that the expected accuracy can be achieved for the developed high-order LSFD-FV method in the 3D case. Moreover, the high-order LSFD-FV method has smaller relative errors than the second-order one, which indicates the higher accuracy of the high-order method on the same mesh. This conclusion can also be visualized through the change curves in Fig. 3. The efficiency comparison shown in Fig. 4 offers evident proof that the high-order LSFD-FV method possesses better computational

TABLE I. Accuracy test of the LSFD-FV method on hexahedral grids for the 3D advection of density perturbation.

Schemes	Grid size	L_2 errors	Order
2nd order LSFD-FV	1/10	2.29×10^{-2}	
	1/15	9.94×10^{-3}	2.054
	1/20	5.58×10^{-3}	2.006
	1/30	2.49×10^{-3}	1.991
3rd order LSFD-FV	1/10	6.98×10^{-3}	
	1/15	2.06×10^{-3}	3.006
	1/20	8.61×10^{-4}	3.041
	1/30	2.51×10^{-4}	3.037

TABLE II. Accuracy test of the LSFD-FV method on tetrahedral grids for the 3D advection of density perturbation.

Schemes	Grid size	L_2 errors	Order
2nd order LSFD-FV	1/5	1.79×10^{-2}	
	1/10	3.32×10^{-3}	2.430
	1/15	1.41×10^{-3}	2.101
3rd order LSFD-FV	1/5	1.39×10^{-2}	
	1/10	1.95×10^{-3}	2.837
	1/15	4.83×10^{-4}	3.443

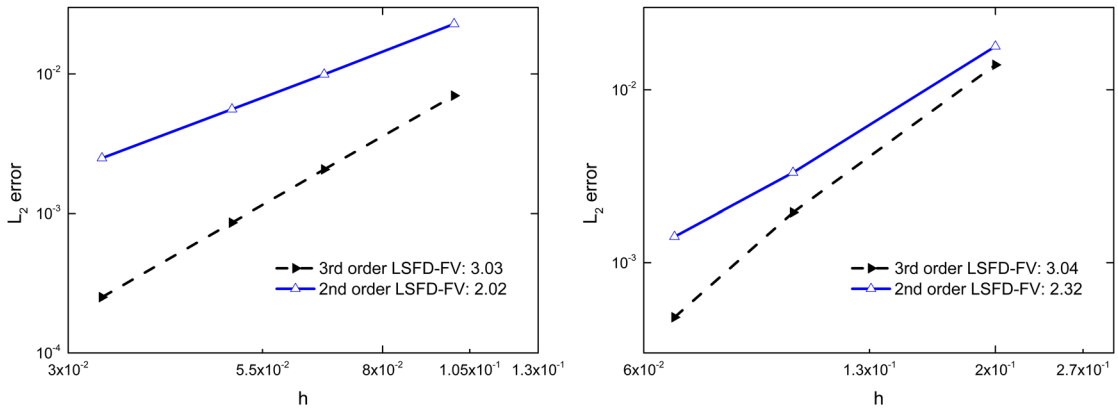

FIG. 3. L_2 error of density on hexahedral mesh (left) and tetrahedral mesh (right) for different schemes.

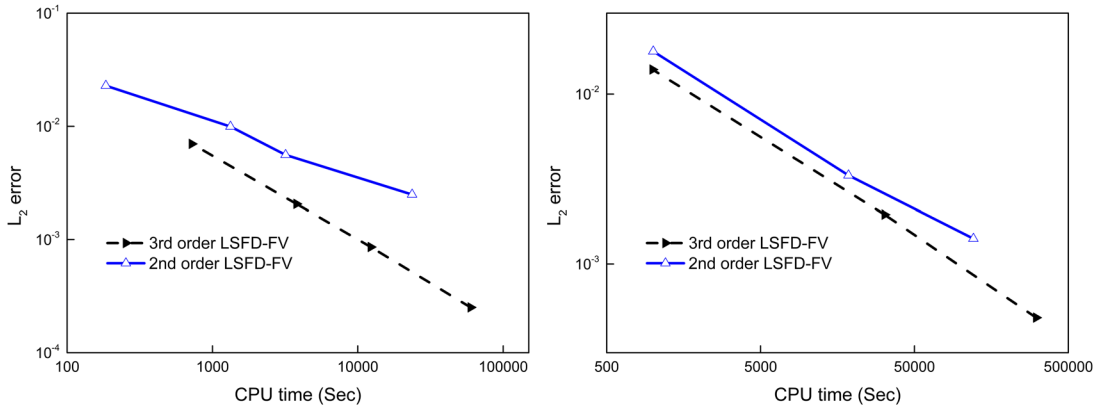

FIG. 4. Efficiency comparison on hexahedral mesh (left) and tetrahedral mesh (right) for different schemes.

efficiency than the second-order one when the same accuracy of the solution is pursued.

B. Lid-driven cavity flow

The lid-driven cavity flow in a cube is then simulated to demonstrate the ability of the present high-order FV method with the LBFS in modeling 3D incompressible viscous flow problems. The physical configuration of this problem is common and can be found in many previous studies.[15,46–48] In this case, the flow is dominated by the Reynolds number defined as $Re = \rho u_0 L/\mu$, where u_0 denotes the velocity of the lid, L is the length of the cubic cavity, and μ refers to the dynamic viscosity. The flow parameters applied in the simulation are given as $\rho = 1$, $u_0 = 0.1$, and $L = 1$. Initially, the dynamic viscosity can be computed from the Reynolds number, and then, the single relaxation parameter can be obtained. Three cases of $Re = 100$, 400, and 1000 are considered here. The $40 \times 40 \times 40$ non-uniform mesh shown in Fig. 5 is used for the simulations at $Re = 100$ and 400. The $60 \times 60 \times 60$ uniform mesh is used for the case at $Re = 1000$.

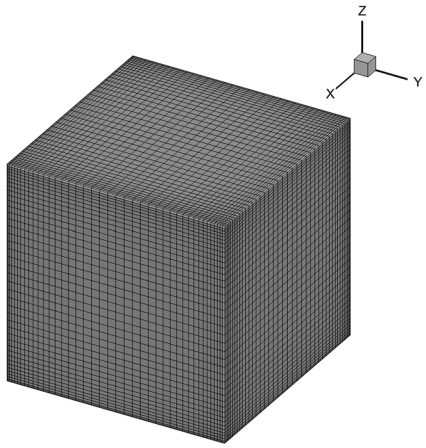

FIG. 5. Mesh used for the three-dimensional lid-driven cavity flow.

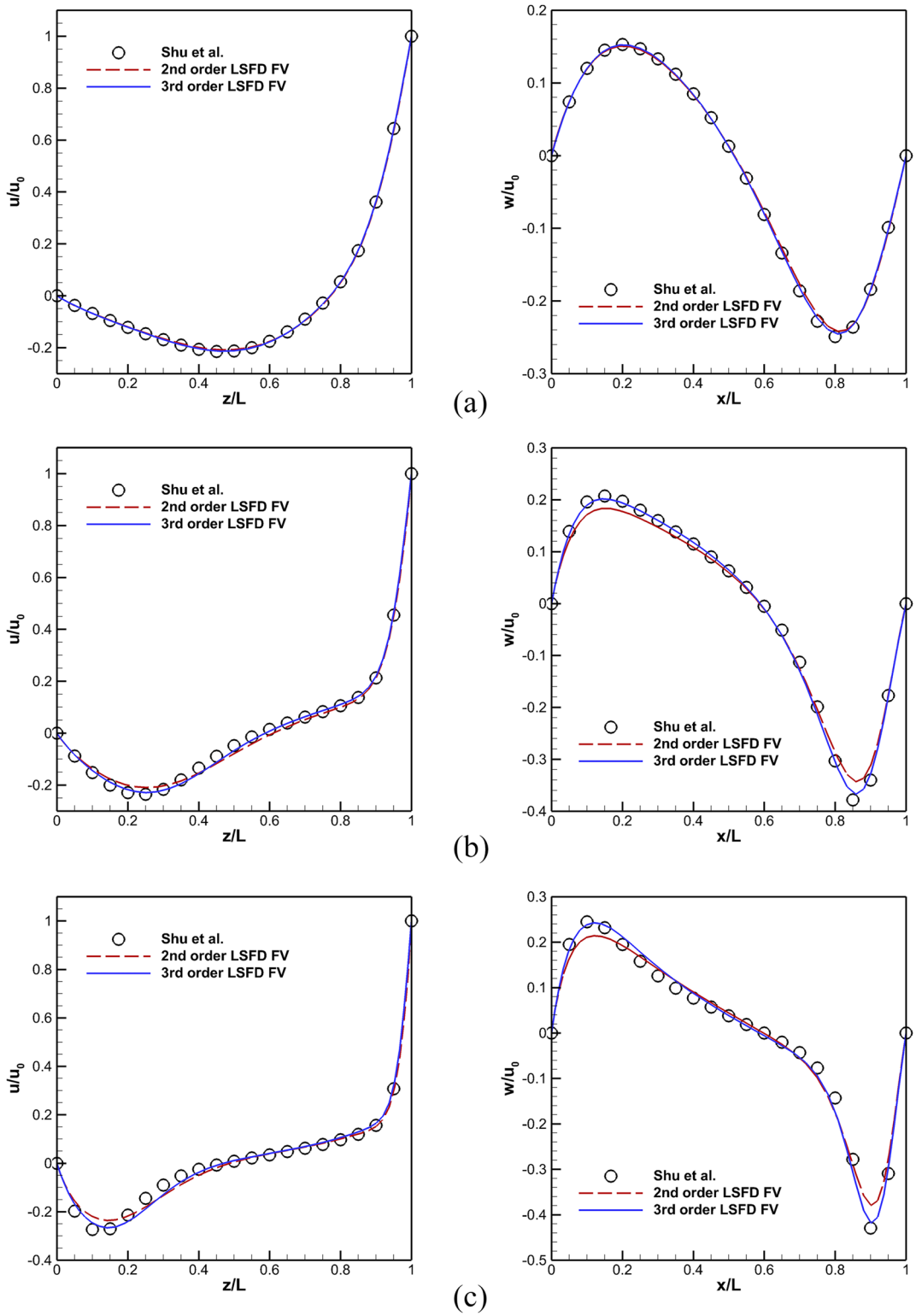

FIG. 6. Three-dimensional lid-driven cavity flow: comparison of the *u*-velocity (left) and *w*-velocity (right) profiles along vertical and horizontal central lines at the *x*–*z* plane with $y = 0$ at (a) $Re = 100$, (b) $Re = 400$, and (c) $Re = 1000$.

The results obtained by the third-order LSFD-FV method are extracted, and the results of Shu *et al.*[46] using the global method of differential quadrature are taken as the benchmark data. In addition, for comparison purposes, the second-order method is also used to simulate the three cases on the same mesh. Figure 6 shows the computed w-velocity profiles along the horizontal centerline and u-velocity profiles along the vertical centerline at the x–z plane with $y = 0.5$ for different Reynolds numbers. Clearly, on the coarse grids, the results obtained by the third-order LSFD-FV method match well with the benchmark data and they are in better agreement with the reference data than those of the second-order method. Moreover, the streamlines calculated by the third-order LSFD-FV method at the y–z plane with $x = 0.5$, x–z plane with $y = 0.5$, and x–y plane with $z = 0.5$ at three different Reynolds numbers are

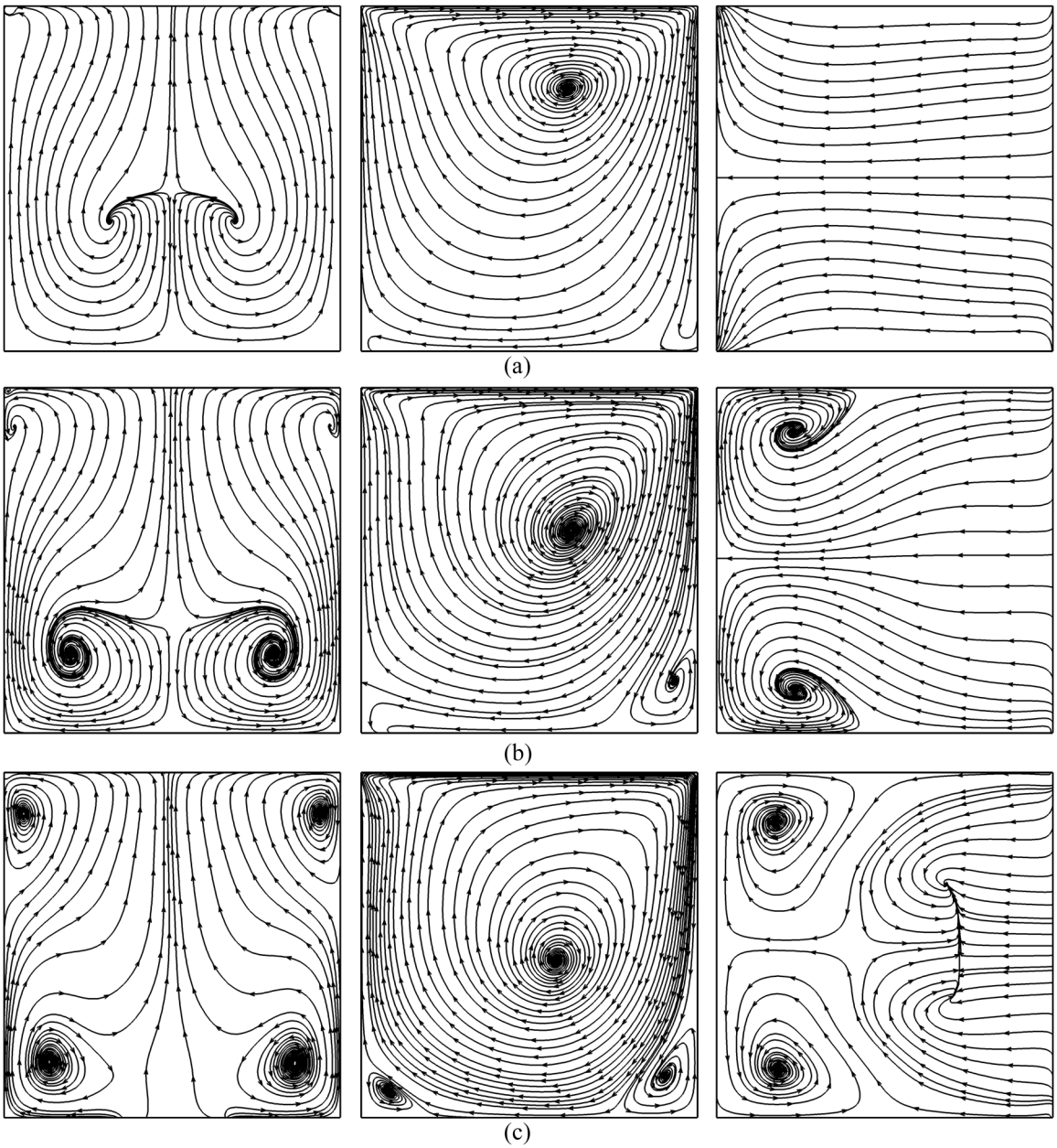

FIG. 7. Three-dimensional lid-driven cavity flow: the streamlines at the y–z plane with $x = 0.5$, x–z plane with $y = 0.5$, and x–y plane with $z = 0.5$ (from left to right) for (a) $Re = 100$, (b) $Re = 400$, and (c) $Re = 1000$.

presented in Fig. 7. It is observed that the flow patterns agree fairly well with those reported in Refs. 15 and 38. Thus, it can be concluded that the present high-order LSFD-FV method can simulate the 3D incompressible viscous flows reliably with the high-order accuracy.

C. Natural convection in a cubic cavity

The natural convection in a cubic cavity serves as a classic benchmark problem in validating the performance of numerical methods for simulation of the 3D thermal flows. In this problem, two vertical walls at $x = 0$ and $x = L$, respectively, have a cool temperature of $T_0 = 0$ and a hot temperature of $T_1 = 1$. Other four walls are adiabatic. The no-slip boundary conditions are applied on all walls. The flow pattern of this test example is governed by two dimensionless parameters, i.e., the Prandtl number Pr and the Rayleigh number Ra. Here, the Rayleigh number Ra is defined as

$$Ra = \frac{g\beta(T_1 - T_0)L^3}{\nu\kappa} = \frac{V_c^2 L^2}{\nu\kappa}, \tag{37}$$

where $V_c = \sqrt{g\beta L\Delta T}$ is the characteristic thermal velocity constrained by the low Mach number limit, ν denotes the kinematic viscosity, g denotes the gravity acceleration, β is the thermal expansion coefficient, and L is the characteristic length of the cubic

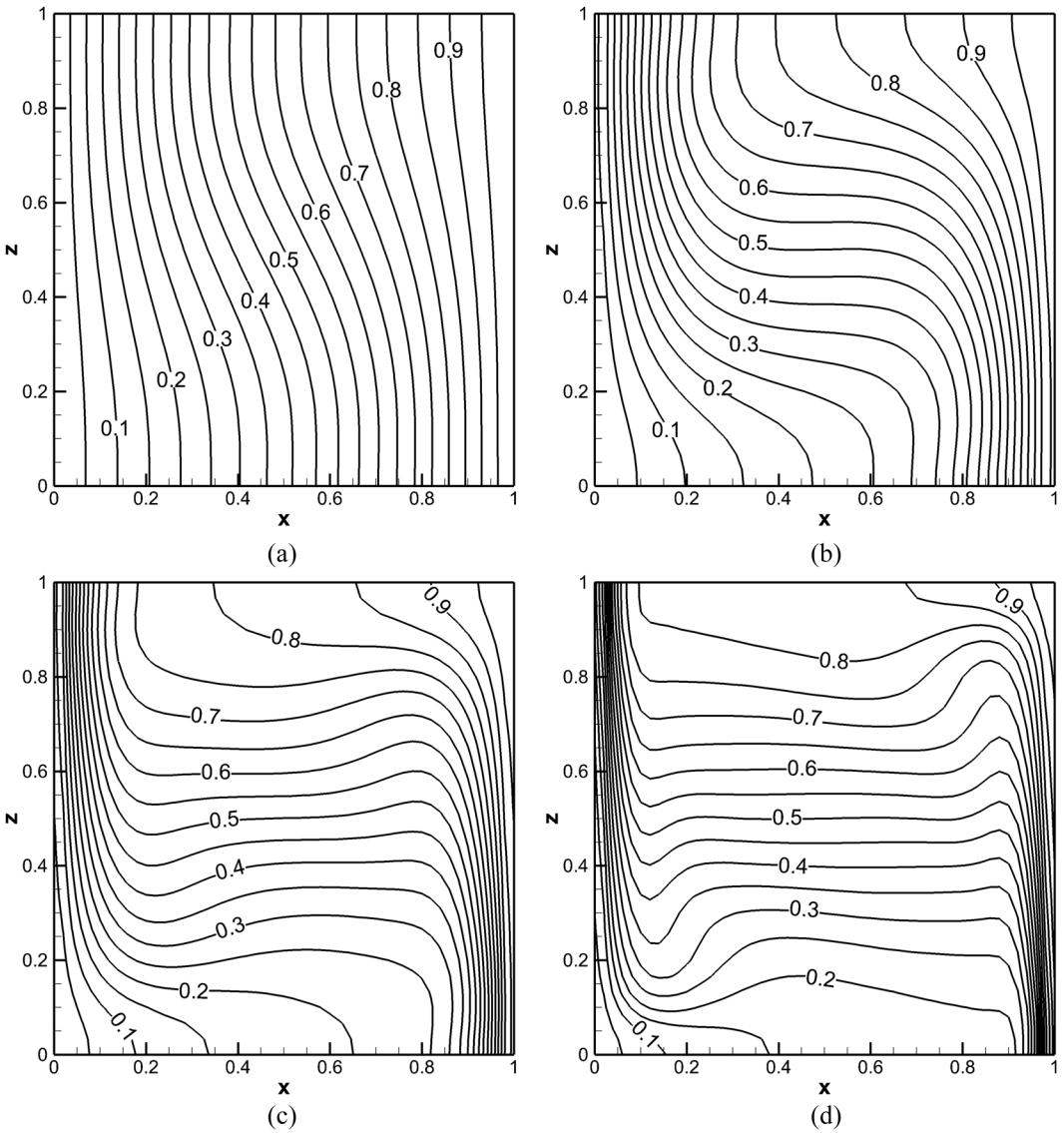

FIG. 8. Temperature contours on the $y = 0.5$ plane for natural convection in a cubic cavity by the high-order LSFD-FV method with LBFS at different Rayleigh numbers: (a) $Ra = 10^3$, (b) $Ra = 10^4$, (c) $Ra = 10^5$, and (d) $Ra = 10^6$.

cavity. The effect of the temperature field on the flow field is considered by the buoyancy force, which is exerted on the momentum equation as a source term $\boldsymbol{Q} = [0, 0, -\rho g\beta(T - T_m), 0]^T$ according to the Boussinesq approximation. T_m is the average temperature of the flow field. For this test case, we set $Pr = 0.71$ and $V_c = 0.1$. Four cases of the Rayleigh number $Ra = 10^3$, 10^4, 10^5, and 10^6 are simulated. All simulations are conducted on a hexahedral mesh with 40 × 30 × 30 cells by the high-order LSFD-FV method with the LBFS for flux evaluation.

The computed isotherms on the $y = 0.5$ plane at various Rayleigh numbers of 10^3–10^6 are visualized in Fig. 8. Denser isotherms squeezed close to the isothermal walls are observed in the case at high Rayleigh numbers, which agrees well with those obtained by Wang *et al.*[38] using the second-order FV method with the LBFS on uniform 80 × 80 × 80 hexahedral grids and Chen *et al.*[49] using the simplified lattice Boltzmann method on non-uniform 80 × 40 × 80 hexahedral grids. These successful predictions of abrupt flow changes by coarse uniform meshes show that the developed high-order LSFD-FV method enjoys higher accuracy than the conventional second-order method. Furthermore, Fig. 9 compares the obtained u—velocity along the vertical centerline and w—velocity along the horizontal centerline on the $y = 0.5$ plane with the results of Yang *et al.*[50] computed by a second-order simple gas-kinetic scheme. Clearly, good agreements are achieved.

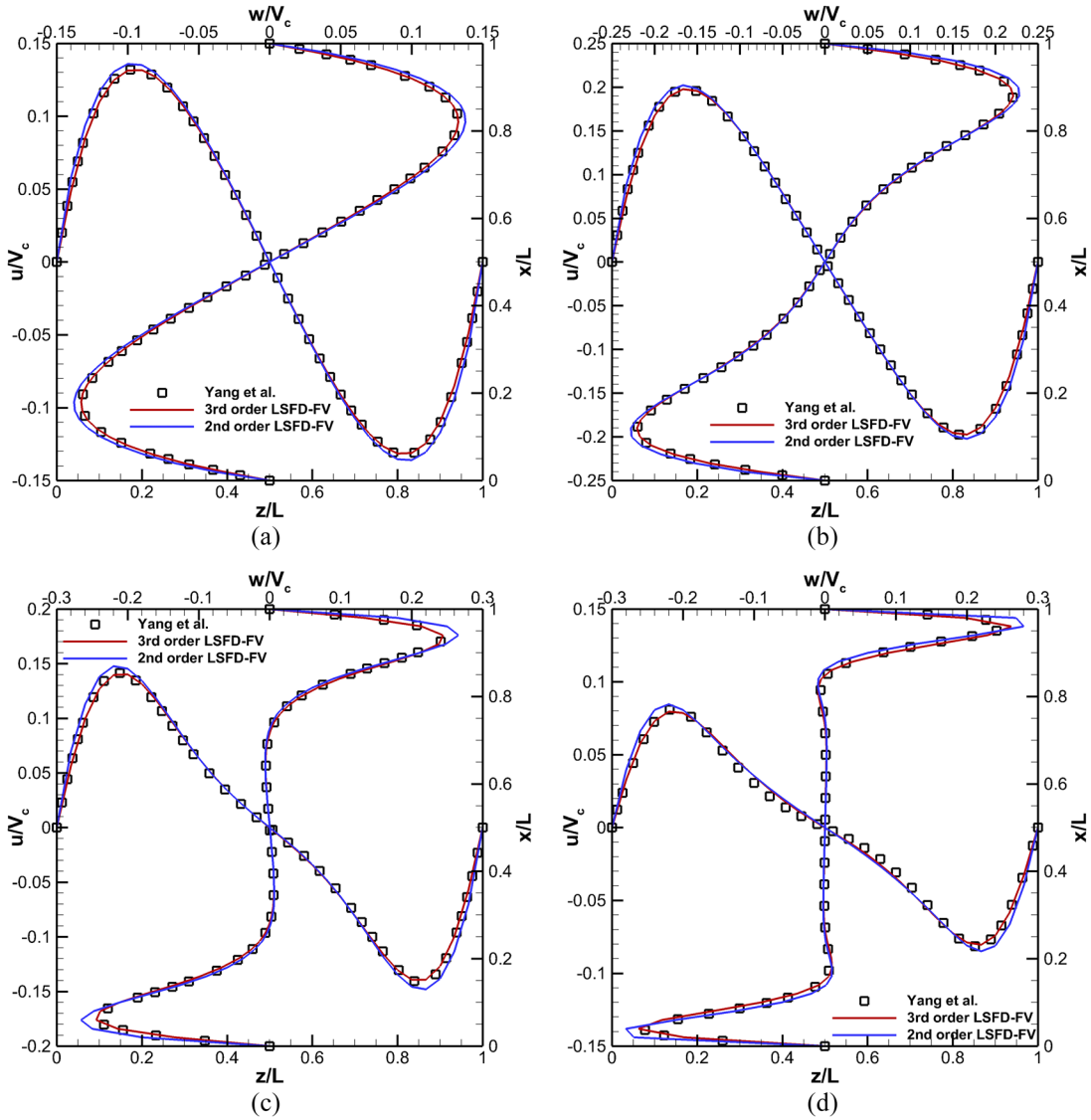

FIG. 9. Comparison of the profiles of u—velocity along the vertical centerline and w—velocity along the horizontal centerline on the $y = 0.5$ plane for natural convection in a cubic cavity by second- and high-order LSFD-FV methods with LBFS at different Rayleigh numbers: (a) $Ra = 10^3$, (b) $Ra = 10^4$, (c) $Ra = 10^5$, and (d) $Ra = 10^6$.

For quantitative comparison, the mean Nusselt number on the $y = 0.5$ plane at the hot wall and the overall Nusselt number at the hot wall defined as follows are compared,

$$Nu_{mean}(y) = \int_0^1 \left.\frac{\partial T(y,z)}{\partial x}\right|_{x=1} dz, \tag{38}$$

$$Nu_{overall} = \int_0^1 Nu_{mean}(y)dy. \tag{39}$$

The detailed comparisons with the reference data reported in the literature[38,50,51] are shown in Table III, where the maximum relative error of the high-order method is found to be within 1.6%. Such a good accordance validates the correctness of the high-order LSFD-FV method in the 3D scenario. In addition, it can be seen from Table III that the high-order LSFD-FV method outperforms the second-order method in terms of the accuracy due to the smaller relative error. Moreover, the comparisons of computational efficiency and memory cost between the high- and second-order methods are presented in Table IV. It can be observed that more than 4 times CPU time and larger virtual memory are required by the second-order method to achieve comparable results of the high-order method. This observation indicates that the high-order LSFD-FV method has better computational efficiency.

D. Flow around ONERA M6 wing

To further quantitatively assess the performance of the present high-order LSFD-FV method in simulating the 3D compressible flow problems with complex configurations, the case of transonic flow around the ONERA M6 wing is tested. In this numerical

TABLE III. Comparison of representative field properties along the symmetric plane at $y = 0.5$ for 3D natural convection at four different Rayleigh numbers: $Ra = 10^3$, 10^4, 10^5, and 10^6. Boldface values denote those computed by the LSFD-FV methods.

		$Ra = 10^3$	$Ra = 10^4$	$Ra = 10^5$	$Ra = 10^6$
$u_{\max}$	Wang *et al.*[38]	0.132	0.200	0.142	0.082
	Yang *et al.*[50]	0.132	0.198	0.142	0.081
	Fusegi *et al.*[51]	0.131	0.201	0.147	0.084
	3rd order LSFD-FV	**0.132**	**0.198**	**0.140**	**0.080**
	2nd order LSFD-FV	**0.136**	**0.202**	**0.148**	**0.085**
Z	Wang *et al.*[38]	0.187	0.176	0.147	0.146
	Yang *et al.*[50]	0.179	0.179	0.142	0.142
	Fusegi *et al.*[51]	0.200	0.183	0.145	0.144
	3rd order LSFD-FV	**0.179**	**0.174**	**0.147**	**0.141**
	2nd order LSFD-FV	**0.167**	**0.174**	**0.133**	**0.141**
$w_{\max}$	Wang *et al.*[38]	0.133	0.221	0.244	0.253
	Yang *et al.*[50]	0.133	0.221	0.245	0.255
	Fusegi *et al.*[51]	0.132	0.225	0.247	0.259
	3rd order LSFD-FV	**0.133**	**0.221**	**0.244**	**0.261**
	2nd order LSFD-FV	**0.138**	**0.228**	**0.266**	**0.280**
x	Wang *et al.*[38]	0.829	0.885	0.932	0.968
	Yang *et al.*[50]	0.821	0.883	0.932	0.957
	Fusegi *et al.*[51]	0.833	0.883	0.935	0.967
	3rd order LSFD-FV	**0.821**	**0.882**	**0.940**	**0.960**
	2nd order LSFD-FV	**0.821**	**0.882**	**0.940**	**0.960**
Nu_{mean}	Wang *et al.*[38]	1.092	2.289	4.622	8.921
	Yang *et al.*[50]	1.088	2.251	4.606	8.771
	Fusegi *et al.*[51]	1.105	2.302	4.646	9.012
	3rd order LSFD-FV	**1.088**	**2.251**	**4.585**	**8.639**
	2nd order LSFD-FV	**1.099**	**2.359**	**5.076**	**10.163**
$Nu_{overall}$	Wang *et al.*[38]	1.071	2.062	4.344	8.684
	Yang *et al.*[50]	1.071	2.055	4.331	8.540
	Fusegi *et al.*[51]	1.085	2.085	4.361	8.770
	3rd order LSFD-FV	**1.071**	**2.056**	**4.319**	**8.432**
	2nd order LSFD-FV	**1.080**	**2.155**	**4.798**	**9.965**

TABLE IV. Comparison of computational cost of the third-order and second-order LSFD-FV methods for natural convection in a cubic cavity at $Ra = 10^4$.

Methods	Third order LSFD-FV	Second order LSFD-FV	Second order LSFD-FV
Grids	40 × 30×30	40 × 30×30	100 × 100×100
Nu_{mean}	2.251	2.359	2.289
$Nu_{overall}$	2.056	2.155	2.090
Virtual memory (Megabytes)	431.5	286.8	1 898.1
Iteration steps	8 544	8617	20 929
Computational time (s)	26 505.9	7697.9	115 629.5

simulation, the free-stream Mach number is 0.84 and the angle of attack is 3.06°. The computational mesh contains 347 718 tetrahedral cells, where 13 236 triangular cells are set on the surfaces of the wing as shown in Fig. 10.

Figure 11 depicts the pressure contours obtained by the present high-order LSFD-FV method. The "λ" shape shock wave on the upper surface of the wing can be clearly seen, which agrees well with the results reported by Yang *et al.*[52] Figure 12 shows the pressure coefficient distributions at selected spanwise locations computed by the high-order LSFD-FV method. The experimental results[53] are also presented in Fig. 12 for comparison. The results of the high-order LSFD-FV method quantitatively agree well with the experimental data. Overall, the above results confirm the capability of the present high-order FV method for simulation of non-smooth compressible inviscid flows with complex geometry.

E. Steady subsonic viscous flow around a sphere

To test the performance of the developed high-order LSFD-FV method in simulating the 3D compressible viscous flows with curved boundaries, the problem of the steady viscous flow around a sphere[54] is solved. The Reynolds number is set to be 118 based on the spherical diameter, and the inlet Mach number is 0.2535, which is in line with the experimental condition[55] and the computational condition.[54,56] The spherical diameter is taken as 1, and the computational domain is a cylinder whose diameter is 10 and height is 25. This computational domain is discretized by 576 631 tetrahedrons, and there are 5574 triangular cells on the walls. The mesh near the sphere is refined, and the corresponding mesh size is set as $h = 0.04$. Figure 13 shows the computational mesh.

Since the flow field in this simulation is smooth, no shock-capturing technique is required. The computations are conducted using the second- and high-order methods with the DGKFS. Figure 14 presents the computed Mach number contours and streamlines near the wake region by the high-order LSFD-FV method. It can be confirmed that the obtained Mach number contours, streamlines, and the size of the separation zone are in good agreement with both the experimental data and the numerical results in the literature shown in Fig. 15. To quantitatively validate the correctness of the computed results, the computed drag coefficients,

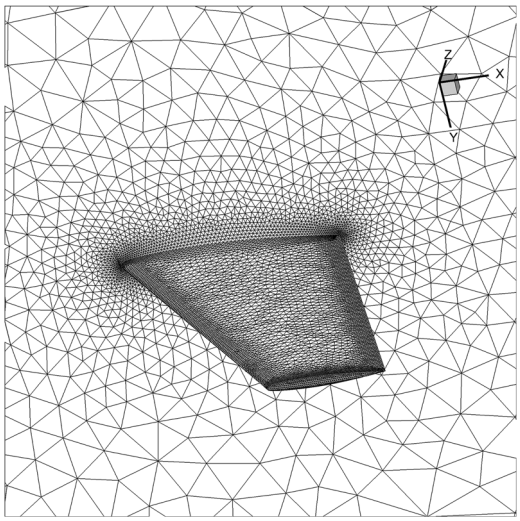

FIG. 10. Unstructured mesh on the walls and symmetry boundary of the ONERA M6 wing.

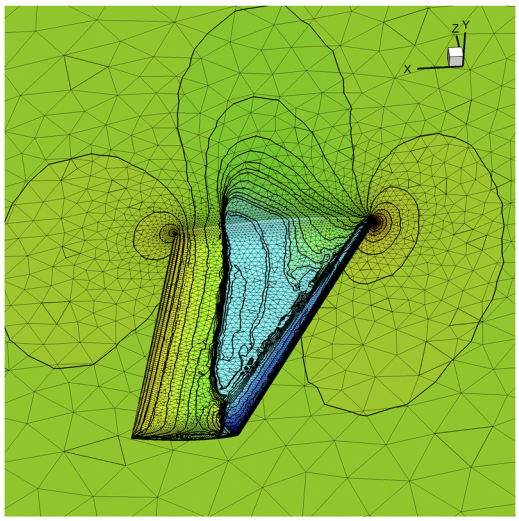

FIG. 11. Pressure contours obtained by the high-order LSFD-FV method for flow around the ONERA M6 wing.

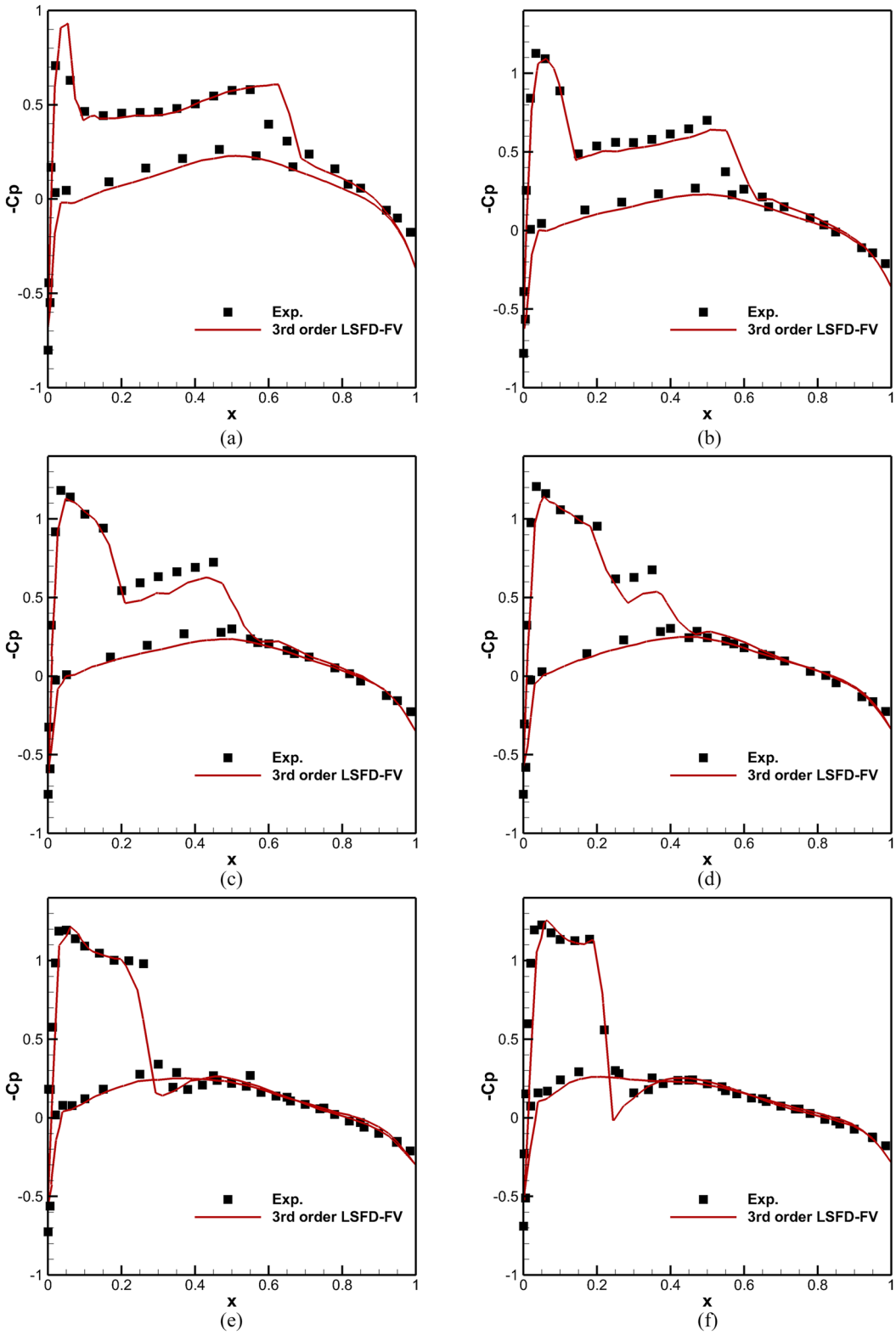

FIG. 12. Comparison of pressure coefficient distributions on the ONERA M6 wing at the (a) 20%, (b) 44%, (c) 65%, (d) 80%, (e) 90%, and (f) 95% spanwise stations.

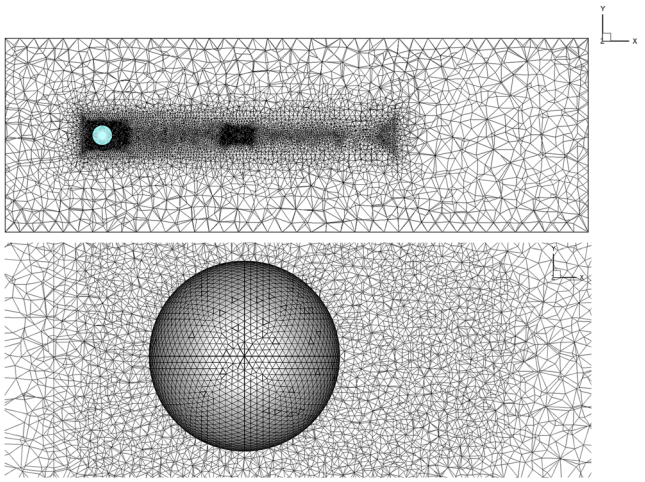

FIG. 13. Computational mesh for the subsonic viscous flow around a sphere. Top: entire mesh; bottom: mesh around the sphere.

predicted separation angle θ_s, and wake length L_s by the second- and high-order methods are compared with the data reported in Refs. 27, 54, 56, and 57. The details are tabulated in Table V, where the results of the high-order scheme agree better with the reference data than the second-order one. This observation validates the correctness and

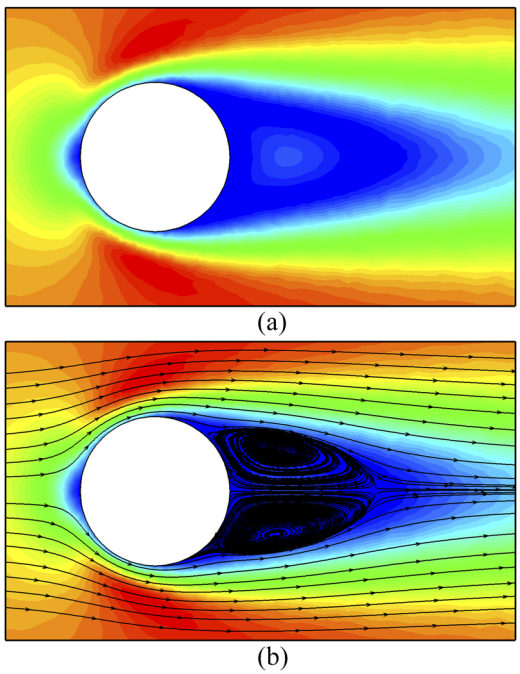

FIG. 14. (a) Mach number contours and (b) streamlines near the wake region obtained by the high-order LSFD-FV method for the steady subsonic viscous flow around a sphere.

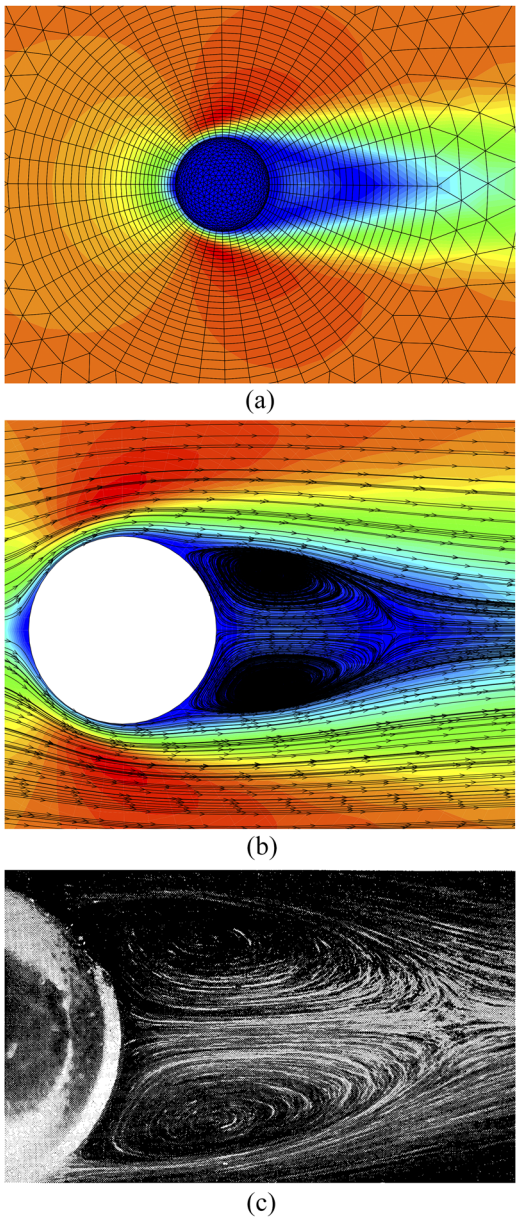

FIG. 15. (a) Mach number contours and (b) streamlines reported in Ref. 56, and (c) streamlines reported in Ref. 55 near the wake region for the steady subsonic viscous flow around a sphere.

robustness of the high-order LSFD-FV method in solving the 3D compressible viscous flow with curved boundaries on unstructured mesh.

F. Steady supersonic viscous flow around a sphere

The supersonic flow around a sphere is further tested to assess the capacity of the current method for capturing the shock wave. In

TABLE V. Comparison of separation angle θ_s, wake length L_s, and drag coefficient C_d for the steady subsonic viscous flow around a sphere. Boldface values denote those computed by the LSFD-FV methods.

Re		C_d	θ_s (deg)	L_s/D
118	Haga *et al.*[54]	...	123.6	...
	Cheng *et al.*[56]	1.0162	123.7	0.96
	Castonguay[57]	1.0162	123.6	...
	Sun *et al.*[27]	...	123.6	1.04
	2nd order LSFD-FV	**1.0245**	**129.3**	**0.94**
	3rd order LSFD-FV	**1.0156**	**123.7**	**0.96**

the simulation, the Reynolds number based on the spherical diameter and the inlet Mach number are 300 and 2, respectively. Under these conditions, as discussed in Ref. 58, the flow field becomes steady and axisymmetric.

Figure 16 presents the flow domain used in the simulation. It is centered around the sphere whose diameter D is 1. The far field boundary is at $24.8D$. There are 362 880 hexahedrons to discretize the flow domain. Near the sphere, the computational grid is refined with a mesh size of $h = 0.023$. No-slip and far field boundary conditions are, respectively, enforced on the sphere and the far field boundaries. In Fig. 17, the streamlines and Mach number contours near the wake region obtained by the high-order LSFD-FV method are depicted. Clearly, stable and axisymmetric flow structures are obtained. To quantitatively assess the results, Table VI compares some characteristic parameters computed by the present high-order method, i.e., the drag coefficient C_d, shock stand-off distance L_{ssd}, separation angle θ_s, and wake length L_s, with those in the literature.[58–60] It is observed that the results are in good agreement. These outcomes well validate the capability of the current method for capturing the shock waves in supersonic flow problems.

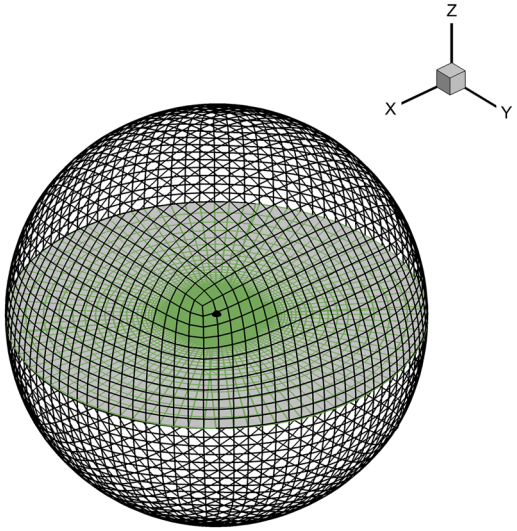

FIG. 16. Computational mesh for the supersonic viscous flow around a sphere.

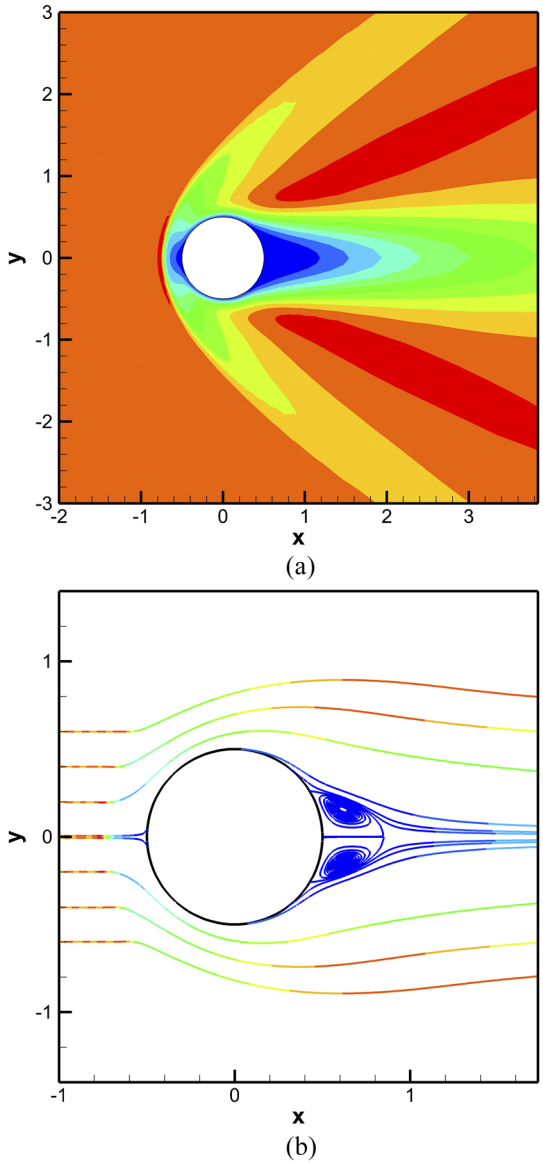

FIG. 17. (a) Mach number contours and (b) streamlines near the wake region in the x–y plane obtained by the high-order LSFD-FV method for the steady supersonic viscous flow around a sphere.

TABLE VI. Comparison of drag coefficient C_d, shock stand-off distance L_{ssd}, separation angle θ_s, and wake length L_s for the steady supersonic viscous flow around a sphere. Boldface values denote those computed by the LSFD-FV methods.

Re		C_d	L_{ssd}	θ_s (deg)	L_s/D
300	Nagata *et al.*[58]	1.387	0.20	150.0	0.36
	Riahi *et al.*[59]	1.41	0.20	...	0.5
	Nagata *et al.*[60]	1.452	...	148.6	0.39
	3rd order LSFD-FV	**1.395**	**0.21**	**149.7**	**0.36**

IV. CONCLUSIONS

In this paper, a 3D high-order least square-based finite difference-finite volume method on unstructured grids is proposed for incompressible and compressible flows. This 3D LSFD-FV method directly applies a Taylor series expansion within each control cell as the solution approximation polynomial. The unknown derivatives are approximated by the mesh-free LSFD scheme. Due to such straightforward and simple approaches of solution approximation and derivative approximation, the resultant LSFD-FV method is user-friendly and easy to implement. Various flux solvers are adopted to evaluate the fluxes at the cell interface. Especially for simulations of incompressible and compressible viscous flows, the LBFS and GKFS are, respectively, applied. In this process, the inviscid and viscous fluxes are simultaneously computed, which avoids additional treatments for the viscous discretization. This makes the LSFD-FV method be competitive in simulating viscous flow problems. Due to the application of the mesh-free LSFD method and flux solvers at each cell interface, the LSFD-FV method is flexible for solving problems with complex geometries on unstructured grids.

The performance of the 3D high-order LSFD-FV method is examined systematically by representative incompressible and compressible benchmark cases. First, the third-order of accuracy is validated on both hexahedral and tetrahedral grids. Second, the numerical results of the high-order LSFD-FV method agree better with the benchmark data than the conventional low-order method on the same grids. Additionally, the present high-order method outperforms the low-order one in terms of computational efficiency. For instance, for natural convection in a cubic cavity at $Ra = 10^4$, the high-order LSFD-FV method takes only about 22.9% computational time and 22.7% virtual memory of the low-order method to get converged results. Furthermore, the present high-order method successfully simulates the compressible flows with complex geometries on relatively coarse tetrahedral grids, which demonstrates its capability of handling unstructured mesh. Given the performance stated above, this 3D high-order LSFD-FV method looks promising in practical problems of engineering interest.

DATA AVAILABILITY

The data that support the findings of this study are available within the article.

REFERENCES

[1] O. V. Vasilyev, "High order finite difference schemes on non-uniform meshes with good conservation properties," J. Comput. Phys. **157**, 746–761 (2000).

[2] Z. F. Tian and Y. B. Ge, "A fourth-order compact finite difference scheme for the steady stream function-vorticity formulation of the Navier-Stokes/Boussinesq equations," Int. J. Numer. Methods Fluids **41**, 495–518 (2003).

[3] W. S. Don, P. Li, K. Y. Wong, and Z. Gao, "Improved symmetry property of high order weighted essentially non-oscillatory finite difference schemes for hyperbolic conservation laws," Adv. Appl. Math. Mech. **10**, 1418–1439 (2018).

[4] M. Sari, G. Gürarslan, and A. Zeytinoğlu, "High-order finite difference schemes for solving the advection-diffusion equation," Math. Comput. Appl. **15**, 449–460 (2010).

[5] C.-W. Shu and S. Osher, "Efficient implementation of essentially non-oscillatory shock-capturing schemes," J. Comput. Phys. **77**, 439–471 (1988).

[6] G.-S. Jiang and C.-W. Shu, "Efficient implementation of weighted ENO schemes," J. Comput. Phys. **126**, 202–228 (1996).

[7] J. Liu, J. Qiu, O. Hu, N. Zhao, M. Goman, and X. Li, "Adaptive Runge-Kutta discontinuous Galerkin method for complex geometry problems on Cartesian grid," Int. J. Numer. Methods Fluids **73**, 847–868 (2013).

[8] O. Friedrich, "Weighted essentially non-oscillatory schemes for the interpolation of mean values on unstructured grids," J. Comput. Phys. **144**, 194–212 (1998).

[9] C. Hu and C.-W. Shu, "Weighted essentially non-oscillatory schemes on triangular meshes," J. Comput. Phys. **150**, 97–127 (1999).

[10] T. J. Barth and P. O. Frederickson, "Higher order solution of the Euler equations on unstructured grids using quadratic reconstruction," AIAA Paper No. 90-0013, 1990.

[11] T. J. Barth, "Recent developments in high-order k-exact reconstruction on unstructured meshes," AIAA Paper No. 93-0668, 1993.

[12] C. Ollivier-Gooch and M. Van Altena, "A high-order-accurate unstructured mesh finite-volume scheme for the advection-diffusion equation," J. Comput. Phys. **181**, 729–752 (2002).

[13] L. Cueto-Felgueroso, I. Colominas, X. Nogueira, F. Navarrina, and M. Casteleiro, "Finite volume solvers and moving least-squares approximations for the compressible Navier-Stokes equations on unstructured grids," Comput. Methods Appl. Mech. Eng. **196**, 4712–4736 (2007).

[14] Y. Guo, L. Tang, H. Zhang, and S. Song, "A maximum-principle-preserving third order finite volume SWENO scheme on unstructured triangular meshes," Adv. Appl. Math. Mech. **10**, 114–137 (2018).

[15] L. Pan and K. Xu, "A third-order gas-kinetic scheme for three-dimensional inviscid and viscous flow computations," Comput. Fluids **119**, 250–260 (2015).

[16] L. Pan and K. Xu, "Two-stage fourth-order gas-kinetic scheme for three-dimensional Euler and Navier-Stokes solutions," Int. J. Comput. Fluid Dyn. **32**, 395–411 (2018).

[17] Q. Wang, Y.-X. Ren, J. Pan, and W. Li, "Compact high order finite volume method on unstructured grids III: Variational reconstruction," J. Comput. Phys. **337**, 1–26 (2017).

[18] W. H. Reed and T. R. Hill, "Triangular mesh methods for the neutron transport equation," Technical Report LA-UR-73-479, Los Alamos Scientific Laboratory, Los Alamos, 1973.

[19] B. Cockburn and C.-W. Shu, "TVB Runge-Kutta local projection discontinuous Galerkin finite element method for conservation laws II: General framework," Math. Comput. **52**, 411–435 (1989).

[20] B. Cockburn and C.-W. Shu, "The Runge-Kutta discontinuous Galerkin method for conservation laws V: Multidimensional systems," J. Comput. Phys. **141**, 199–224 (1998).

[21] J. Cheng, H. Yue, S. Yu, and T. Liu, "A direct discontinuous Galerkin method with interface correction for the compressible Navier-Stokes equations on unstructured grids," Adv. Appl. Math. Mech. **10**, 1–21 (2018).

[22] F. Bassi and S. Rebay, "A higher-order accurate discontinuous finite element method for the numerical solution of the compressible Navier-Stokes equations," J. Comput. Phys. **131**, 267–279 (1997).

[23] Z. J. Wang and Y. Liu, "Spectral (finite) volume method for conservation laws on unstructured grids IV: Extension to two dimensional systems," J. Comput. Phys. **194**, 716–741 (2004).

[24] Z. J. Wang and Y. Liu, "Spectral (finite) volume method for conservation laws on unstructured grids VI: Extension to viscous flow," J. Comput. Phys. **215**, 41–58 (2006).

[25] Z. J. Wang, "Spectral (finite) volume method for conservation laws on unstructured grids: Basic formulation," J. Comput. Phys. **178**, 210–251 (2002).

[26] Z. J. Wang, Y. Liu, G. May, and A. Jameson, "Spectral difference method for unstructured grids II: Extension to the Euler equations," J. Sci. Comput. **32**, 45–71 (2007).

[27] Y. Z. Sun, Z. J. Wang, and Y. Liu, "High-order multidomain spectral difference method for the Navier-Stokes equations on unstructured hexahedral grids," Commun. Comput. Phys. **2**, 310–333 (2007).

[28] Z. J. Wang, "High-order methods for the Euler and Navier-Stokes equations on unstructured grids," Prog. Aerosp. Sci. **43**, 1–41 (2007).

[29] Y. Y. Liu, C. Shu, H. W. Zhang, and L. M. Yang, "A high order least square-based finite difference-finite volume method with lattice Boltzmann flux solver

for simulation of incompressible flows on unstructured grids," J. Comput. Phys. **401**, 109019 (2019).
[30]Y. Y. Liu, H. W. Zhang, L. M. Yang, and C. Shu, "High-order least-square-based finite-difference–finite-volume method for simulation of incompressible thermal flows on arbitrary grids," Phys. Rev. E **100**, 063308 (2019).
[31]H. Ding, C. Shu, and K. S. Yeo, "Development of least square-based two-dimensional finite difference schemes and their application to simulate natural convection in a cavity," Comput. Fluids **33**, 137–154 (2004).
[32]H. Ding, C. Shu, K. S. Yeo, and D. Xu, "Simulation of incompressible viscous flows past a circular cylinder by hybrid FD scheme and meshless least square-based finite difference method," Comput. Methods Appl. Mech. Eng. **193**, 727–744 (2004).
[33]Y. Sun and Z. J. Wang, "Formulations and analysis of the spectral volume method for the diffusion equation," Commun. Numer. Methods Eng. **20**, 927–937 (2004).
[34]J. J. Douglas and T. Dupont, *Interior Penalty Procedures for Elliptic and Parabolic Galerkin Methods*, Lecture Notes in Physics (Springer, Berlin, 1976), Vol. 58.
[35]B. Cockburn and C.-W. Shu, "The local discontinuous Galerkin method for time-dependent convection-diffusion systems," SIAM J. Numer. Anal. **35**, 2440–2463 (1998).
[36]F. Bassi and S. Rebay, "GMRES discontinuous Galerkin solution of the compressible Navier-Stokes equations," in *Lecture Note in Computational Science and Engineering* (Springer-Verlag, New York, 2000), Vol. 11, pp. 197–208.
[37]F. Bassi, A. Crivellini, S. Rebay, and M. Savini, "Discontinuous Galerkin solution of the Reynolds-averaged Navier-Stokes and k-ω turbulence model equations," Comput. Fluids **34**, 507–540 (2005).
[38]Y. Wang, C. Shu, C. J. Teo, J. Wu, and L. M. Yang, "Three-dimensional lattice Boltzmann flux solver and its applications to incompressible isothermal and thermal flows," Commun. Comput. Phys. **18**, 593–620 (2015).
[39]L. M. Yang, C. Shu, and J. Wu, "A moment conservation-based non-free parameter compressible lattice Boltzmann model and its application for flux evaluation at cell interface," Comput. Fluids **79**, 190–199 (2013).
[40]L. M. Yang, C. Shu, and J. Wu, "Extension of lattice Boltzmann flux solver for simulation of 3D viscous compressible flows," Comput. Math. Appl. **71**, 2069–2081 (2016).
[41]L. M. Yang, C. Shu, Y. Wang, and Y. Sun, "Development of discrete gas kinetic scheme for simulation of 3D viscous incompressible and compressible flows," J. Comput. Phys. **319**, 129–144 (2016).
[42]D. Zhou, Z. Lu, and T. Guo, "A rotating reference frame-based lattice Boltzmann flux solver for simulation of turbomachinery flows," Int. J. Numer. Methods Fluids **83**, 561–582 (2017).
[43]H. Z. Yuan, Y. Wang, and C. Shu, "An adaptive mesh refinement-multiphase lattice Boltzmann flux solver for simulation of complex binary fluid flows," Phys. Fluids **29**, 123604 (2017).
[44]L. Yang, Y. Wang, Z. Chen, and C. Shu, *Lattice Boltzmann and Gas Kinetic Flux Solvers: Theory and Applications* (World Scientific, 2020).
[45]L. Pan and K. Xu, "High-order gas-kinetic scheme with three-dimensional WENO reconstruction for the Euler and Navier-Stokes solutions," Comput. Fluids **198**, 104401 (2020).
[46]C. Shu, L. Wang, and Y. T. Chew, "Numerical computation of three-dimensional incompressible Navier-Stokes equations in primitive variable form by DQ method," Int. J. Numer. Methods Fluids **43**, 345–368 (2003).
[47]H. Ding, C. Shu, K. S. Yeo, and D. Xu, "Numerical computation of three-dimensional incompressible viscous flows in the primitive variable form by local multiquadric differential quadrature method," Comput. Methods Appl. Mech. Eng. **195**, 516–533 (2006).
[48]Z. Chen, C. Shu, and D. Tan, "Highly accurate simplified lattice Boltzmann method," Phys. Fluids **30**, 103605 (2018).
[49]Z. Chen, C. Shu, and D. Tan, "Three-dimensional simplified and unconditionally stable lattice Boltzmann method for incompressible isothermal and thermal flows," Phys. Fluids **29**, 053601 (2017).
[50]L. M. Yang, C. Shu, W. M. Yang, and J. Wu, "A simple gas kinetic scheme for simulation of 3D incompressible thermal flows," Numer. Heat Transfer, Part B **72**, 450–468 (2017).
[51]T. Fusegi, J. M. Hyun, K. Kuwahara, and B. Farouk, "A numerical study of three-dimensional natural convection in a differentially heated cubical enclosure," Int. J. Heat Mass Transfer **34**, 1543–1557 (1991).
[52]L. M. Yang, C. Shu, and J. Wu, "A three-dimensional explicit sphere function-based gas-kinetic flux solver for simulation of inviscid compressible flows," J. Comput. Phys. **295**, 322–339 (2015).
[53]V. Schmitt and F. Charpin, "Pressure distributions on the ONERA-M6-wing at transonic Mach numbers," Experimental Data Base for Computer Program Assessment, Report of the Fluid Dynamics Panel Working Group 04, AGARD AR 138, 1979.
[54]T. Haga, H. Gao, and Z. J. Wang, "A high-order unifying discontinuous formulation for the Navier-Stokes equations on 3D mixed grids," Math. Modell. Nat. Phenom. **6**, 28–56 (2011).
[55]S. Taneda, "Experimental investigation of the wake behind a sphere at low Reynolds numbers," J. Phys. Soc. Jpn. **11**, 1104–1108 (1956).
[56]J. Cheng, X. Liu, T. Liu, and H. Luo, "A parallel, high-order direct discontinuous Galerkin method for the Navier-Stokes equations on 3D hybrid grids," Commun. Comput. Phys. **21**, 1231–1257 (2017).
[57]P. Castonguay, "High-order energy stable flux reconstruction schemes for fluid flow simulations on unstructured grids," Ph.D. thesis, Stanford University, 2012.
[58]T. Nagata, T. Nonomura, S. Takahashi, Y. Mizuno, and K. Fukuda, "Investigation on subsonic to supersonic flow around a sphere at low Reynolds number of between 50 and 300 by direct numerical simulation," Phys. Fluids **28**, 056101 (2016).
[59]H. Riahi, M. Meldi, J. Favier, E. Serre, and E. Goncalves, "A pressure-corrected immersed boundary method for the numerical simulation of compressible flows," J. Comput. Phys. **374**, 361–383 (2018).
[60]T. Nagata, T. Nonomura, S. Takahashi, and K. Fukuda, "Direct numerical simulation of subsonic, transonic and supersonic flow over an isolated sphere up to a Reynolds number of 1000," J. Fluid Mech. **904**, A36 (2020).